Penetration of interferometric radar signals in Antarctic snow

Helmut Rott[1,2 *], Stefan Scheiblauer[1], Jan Wuite[1], Lukas Krieger[3], Dana Floricioiu[3], Paola Rizzoli[4], Ludivine Libert[1], Thomas Nagler[1]

[1] ENVEO IT GmbH, Innsbruck, Austria
[2] Department of Atmospheric and Cryospheric Sciences, Univ. of Innsbruck, Innsbruck, Austria
[3] Remote Sensing Technology Institute, DLR, Oberpfaffenhofen, Germany
[4] Microwaves and Radar Institute, DLR, Oberpfaffenhofen, Germany

* Correspondence to: Helmut Rott (helmut.rott@enveo.at)

Abstract. Synthetic aperture radar interferometry (InSAR) is an efficient technique for mapping the surface elevation and its temporal change over glaciers and ice sheets. However, due to the penetration of the SAR signal into snow and ice the apparent elevation in uncorrected InSAR digital elevation models (DEMs) is displaced versus the actual surface. We studied relations between interferometric radar signals and physical snow properties and tested procedures for correcting the elevation bias. The work is based on satellite and in-situ data over Union Glacier in the Ellsworth Mountains, West Antarctica, including interferometric data of the TanDEM-X mission, topographic data from optical satellite sensors and field measurements on snow structure and stratigraphy undertaken in December 2016. The study area comprises ice-free surfaces, bare ice, dry snow and firn with a variety of structural features related to local differences in wind exposure and snow accumulation. Time series of laser measurements of NASA's Ice, Cloud and land Elevation Satellite (ICESat) and ICESat-2 show steady state surface topography. For area-wide elevation reference we use the Reference Elevation Model of Antarctica (REMA). The different elevation data are vertically co-registered on a blue ice area ~~and an ice-free slope, surfaces~~that is not affected by radar signal penetration. ~~The b~~Backscatter simulations with a multi-layer radiative transfer model show large variations for scattering of individual snow layers ~~due to different size and structure of the scattering elements.~~but the vertical backscatter distribution ~~The average depth-dependent backscatter contributions~~ can be approximated by an exponential function representing uniform absorption and scattering properties. We obtain estimates of the elevation bias by inverting the interferometric volume correlation coefficient (coherence) applying a uniform volume model for describing the vertical loss function. Whereas the mean values of the computed elevation bias and the elevation difference between the ~~TDM~~ TanDEM-X DEMs and the REMA show good agreement, a trend towards overestimation of penetration is evident for heavily wind-exposed areas with low accumulation and towards underestimation for areas with higher accumulation rates. In both cases deviations from the uniform volume structure are the main reason. In the first case the dense sequence of horizontal structures related to internal wind crust, ice layers and density stratification causes increased scattering in near-surface layers. In the second case the small grain size of the top snow layers causes a downward shift of the scattering phase centre.~~The angular gradients of the backscatter intensity show also distinct differences between these two domains. This behaviour can be attributed to the anisotropy of the snow/firn volume structure showing differences in the size and shape of the scattering elements and in stratification related to snow accumulation and wind-driven erosion and deposition~~

1. Introduction

Digital elevation models (DEMs) derived from across-track interferometric synthetic aperture radar (InSAR) data are a main data source for mapping the surface elevation and its temporal change over glaciers and ice sheets. Single-pass (SP) InSAR systems, such as the TanDEM-X (TDM) mission, are of particular interest for this task as they are not affected by variations in the atmospheric phase delay, ice motion and temporal decorrelation. For the analysis and interpretation of InSAR elevation over snow and ice the effects of signal penetration have to be taken into account. The surface inferred from uncorrected InSAR elevation data refers to the position of the scattering phase centre in the snow/firn medium, resulting in an elevation bias versus the actual surface (Dall, 2007). The position and strength of scattering sources in the snow volume and the absorption and scattering losses are main factors defining the depth of the phase centre below the snow surface. Backscatter contributions from sources in different depths within a volume scattering medium, observed under ~~slightly~~ different incidence angles, are causing ~~a spectral wavenumber shift and~~ decorrelation, depending on the interferometric baseline and incidence angle (~~Gatelli et al., 1994~~Bamler and Hartl, 1988).

Hoen and Zebker (2000, 2001) derived a formulation for estimating the power-penetration depth in dry snow from the interferometric coherence, applying a radiative transfer model for estimating spatial decorrelation in a volume of uniformly distributed and uncorrelated scatterers characterized by exponential extinction. They applied this formulation to derive the C-band penetration depth for different sites in Greenland from the coherence of 3-day repeat-pass InSAR data of the ERS-1 SAR mission. Forsberg et al. (2000) and Dall et al. (2001) compared surface elevation measured by airborne laser altimetry and C-band single-pass SAR interferometry on the Geiki ice cap in Greenland. They report zero InSAR elevation bias for wet snow and an average bias of about 10 m for dry snow and firn. Dall (2007) studied relations between the InSAR elevation bias and the power penetration depth in uniform volumes. He shows that the depth of the mean phase centre in a volume scattering medium is approximately equal to the two-way penetration depth if the latter is smaller than about 10% of the height of ambiguity (H_a), the height difference for a phase shift of 2π. Fischer et al. (2019a; 2019b; 2020) studied various concepts for characterizing and modelling the vertical backscatter distribution and retrieving the InSAR penetration bias in the percolation zone of Greenland based on airborne polarimetric multi-baseline InSAR data and in situ measurements of snow structural properties.

In recent years SP-InSAR data of the TDM mission were widely applied for mapping surface elevation and elevation change on glaciers and ice sheets. The TDM mission employs a bi-static interferometric configuration of the two satellites TerraSAR-X and TanDEM-X flying in close formation in order to form a single-pass SAR interferometer (Krieger et al., 2013). Rizzoli et al. (2017a) compared surface elevation over Greenland measured by NASA's Ice, Cloud and land Elevation Satellite (ICESat) laser altimeter with the TanDEM-X global ~~digital elevation model (~~DEM~~)~~. They report for frozen snow and firn in the wet snow zone, the lower and upper percolation zone, and the dry snow zone mean values of the X-band InSAR penetration bias of 3.7 m, 3.9 m, 4.7 m, and 5.4 m, respectively. Abdullahi et al. (2019) use a linear regression model for estimating the elevation bias in TDM DEMs of northern Greenland. The model is based on empirical relations between coherence and backscatter intensity with the difference between the uncorrected TDM DEM and airborne laser altimeter surface heights.

The complex layered structure of polar snow and firn has a major impact on radar signal propagation and interferometric coherence, an obstacle for establishing a generally applicable, physically-based method for estimating the elevation bias of InSAR products. The work presented in this paper takes on this open issue,

exploring relations between interferometric parameters and physical snow properties and investigating the feasibility of deducing the elevation bias from the interferometric correlation. The study is based on interferometric data of the TDM mission, data from optical satellite sensors and field measurements undertaken in December 2016 on Union Glacier in the Ellsworth Mountains, Antarctica. Logistic support was provided by the private company Antarctic Logistics & Expeditions LLC (ALE) which conducts aircraft flights ~~from Punta Arenas, Chile,~~ to Union Glacier and operates in summer a ~~well-equipped~~ field station ~~and logistic facilities~~. The study area comprises ice-free surfaces, bare ice and dry snow and firn exhibiting a diversity of structural features attributed to local differences in wind exposure and snow accumulation. Time series of ICESat laser measurements from 2003 to 2009 and ICESat-2 data show near steady state surface topography, facilitating the intercomparison of TDM and optical elevation data.

In Sect. 2 we describe the study area, present details on the satellite data base and give an account on the structure and morphology of snow and firn at different sites. Sect. 3 explains the basic concept relating the elevation bias and interferometric coherence in a uniform random volume.~~approach for the vertical co-registration of the different DEMs. Furthermore, checks on the temporal stability of surface elevation are presented based on altimetric time series.~~ Sect. 4 ~~reports on the~~deals with vertical co-registration of the different DEMs, including an analysis of the temporal stability of surface elevation, and describes the observed spatial pattern of backscatter signals, coherence and elevation bias. ~~vertical backscatter distribution in snow/firn volumes and presents the theoretical relation between volumetric coherence and the InSAR elevation bias. Sect. 5 shows the spatial patterns of backscattering, coherence and the elevation bias of the different TDM scenes and explains the interdependencies between these parameters.~~ Sect. ~~5~~6 ~~deals with~~presents results of the inversion of the volumetric coherence in terms of the InSAR elevation bias and compares the retrieved bias with elevation differences between TDM DEMs and optical data. ~~In~~ Sect. 6 includes the discussion and Sect. 7 presents conclusions. ~~7 we discuss merits and constraints of the inversion approach in the context of the study results and address open issues~~. The Appendix shows simulations for vertical backscatter distributions at snow pit sites and compares these with exponential backscatter functions.

2. Study area and data

Union Glacier flows from the ice divide in the Heritage Range, Ellsworth Mountains, down to the Constellation Inlet on Ronne Ice Shelf. The glacier section immediately downstream of the main mountain range is exposed to strong katabatic winds so that bare ice appears on the surface (Fig. 1). The blue ice area (BIA) has a negative specific surface mass balance in the order of several centimetres per year due to sublimation (Rivera et al., 2014). On the BIA an ice runway for landing heavy airplanes on wheels is maintained from November to March. The ALE camp is located 8 km downstream of the ice runway ~~(near P3 in Fig. 1)~~.

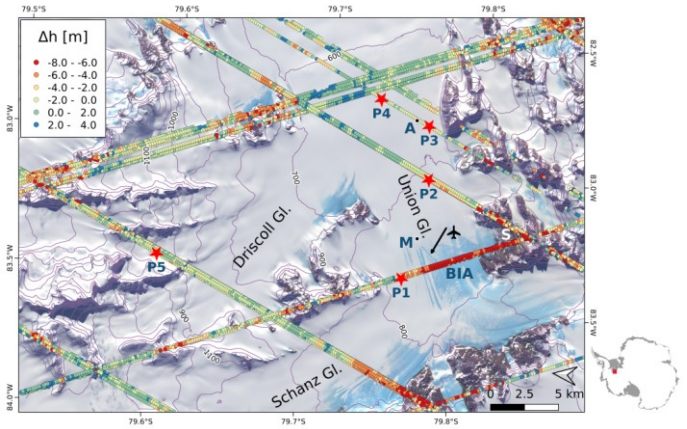

Figure 1. Landsat-8 image acquired on 6 December 2016 (composite of bands 5, 4, 2) with ICESat tracks. Points: elevation difference Δh (ICESat minus TDM global DEM), colour coded from Δh = -8 m to +4 m. P1 to P5: Locations of snow pits. A – ALE camp, BIA – blue ice area, M – recording meteorological station, S – ice free slope. The arrow points to the landing strip.

GPS measurements at stakes, performed during the period 2007 to 2011, show ice velocities in the order of 20 m a^{-1} at the glacier gate across the runway (Rivera et al., 2010; 2014). For 2008 to 2012 a mean wind speed of 16.3 knots with predominant direction from south-west (blowing downstream along the main glacier) was measured at an automatic station close to the runway. Wind speed and direction are very consistent. Rivera et al. (2014) report a mean specific mass balance, b_n, of -0.10 m w.e. a^{-1} measured at 29 stakes on the BIA during 2007 to 2011. The intensity of the katabatic winds declines downstream of the BIA so that snow accumulates and the surface mass balance is positive. Accumulation measurements at 11 stakes up to 15 km downstream of the BIA show a maximum b_n of 0.20 m w.e. a^{-1} at a stake near the ALE camp (Rivera et al., 2014). Hoffmann et al. (2020) collected and analysed six shallow ice cores in the wider Union Glacier region. One of the cores was drilled on Union Glacier itself, about 2 km west of P3, showing for 1989 –to 2013 a mean b_n of 0.18 m w.e. a^{-1}.

Differences in exposure to wind are a main factor for local variations in the accumulation rate and in the structural properties of snow and firn. This is evident in differences of the microstructure and stratigraphy observed in snow pits, ranging from coarse-grained dense snow with wind-crusts near the runway (pit P1), located in the main pathway of the katabatic wind, to finer-grained and softer snow at P5 on a lateral slope of Driscoll Glacier.

Uribe et al. (2014) operated two radar sensors during an oversnow campaign in December 2010, measuring the total ice thickness and the thickness and structure of the firn layers along an 82 km track, starting on Union Glacier and proceeding along Driscoll and Schanz glaciers up to the Ellsworth Plateau. The total thickness of the firn layer varies significantly along this track, even within short distances. For example, a radargram of a 6 km transect extending from the confluence with Driscoll Glacier across Union Glacier towards the camp shows thickness values of the snow/firn layer ranging from zero on blue ice at the confluence of the two glaciers to a maximum of 34 m close to the camp.

2.1 TanDEM-X data

The ~~TanDEM-X~~TDM data for this study comprise one tile of the TDM global (TDMgl) DEM and raw SAR data from several dates for compiling topography, backscatter intensity and coherence products. Tile TDM1_DEM_04_S80W084_V01_C of the global DEM is used, extending from 79° to 80° S and 82° to 84° W and referring to the coordinate reference system WGS84-G1150. This tile was obtained by mosaicking multiple single DEM scenes acquired between 6 May 2013 and 23 August 2014. The pixel spacing is 0.4 arcsec in northing and 1.2 arcsec in easting, corresponding to 12.4 m x 6.5 m at 80° latitude. For the TDMgl elevation products over ice sheets penetration corrections were applied, using ICESat data as elevation reference (Wessel et al., 2016; Rizzoli et al., 2017b). For Antarctica (excluding coastal regions) a mean penetration bias was derived for each of eleven extended homogeneous areas (fixed blocks) located in different sections of the ice sheet. For ~~all other~~the areas in between the elevation is adjusted by spatial interpolation between these blocks, regionally applying bulk values that are not accounting for different surface types (Rizzoli et al., 2017b).

For producing DEMs from raw bistatic SAR data (Level 0) of individual tracks (the so-called Raw DEMs) we used the operational Integrated TanDEM-X Processor (ITP) of the German Aerospace Center (DLR) (Rossi et al., 2012). The Raw DEM pixel spacing is 6 m x 3 m. Complementary to each Raw DEM the ITP provides ~~maps~~ geocoded rasters of the height error, the SAR amplitude, the backscattering coefficient and the interferometric coherence, as well as a flag mask indicating critical areas. We applied 11 x 11 pixels estimation windows for computing the coherence maps, adding up to about 390 independent samples for single-polarized data at 40° incidence angle and about 110 independent samples for dual-polarized data at 22° incidence angle. According to the Cramér-Rao bound for coherence estimation the standard deviation for a coherence magnitude of 0.5 is 0.03 for the first case and 0.05 for the second case. The uncertainty decreases towards higher coherence values (Bamler and Hartl, 1998). The backscatter intensity images are based on absolute radiometric calibration and terrain-corrected geocoding, accounting for the local geocoded incidence angle, antenna beam pattern and correction for thermal noise. The absolute and relative radiometric accuracies for the TerraSAR-X stripmap data are estimated at 0.6 dB and 0.3 dB, respectively (Breit et al., 2010).

The Height Error Map (HEM) delivers the height errors for each DEM pixel caused by random noise. This error is largely driven by the phase uncertainty for which the coherence is the main factor. Low pass filtering is an efficient means for reducing the random height error. The HEM map for the TDMgl DEM of the study region shows over flat terrain and gentle slopes random height errors (standard deviation) ranging from 0.3 m to 1.2 m.

Specifications of the TDM data used in this study are listed in Table 1. The azimuth resolution of the single polarization data is 3.3 m and of the dual polarized data 6.6 m. The ground range resolution is 3.20 m at θ_i = 22° and 1.86 m at θ_i = 40°. We selected scenes with different incidence angles and baselines in order to check the impact of these parameters on coherence, backscatter intensity and signal penetration. According to the HEM maps, the random errors for the Raw DEMs, excluding steep slopes, range from 0.7 m to 3.0 m. The spatial variations can mainly be attributed to phase noise arising from thermal and volume decorrelation. For the estimation of signal penetration we use averages over multiple pixel windows in order to reduce the uncertainty.

Table 1. Specifications of TanDEM-X data used for DEM production and generation of backscatter and coherence images. θ_i is the incidence angle in the scene centre. B_n is the effective interferometric baseline, H_a is the height of ambiguity, k_{zVol} is the vertical interferometric wavenumber in the snow volume assuming a density of 400 kg m^{-3}. SAR operation mode: bistatic.

Label	Date	Rel. Orbit / Scene	Look direction	Polarisation	θ_i [deg]	B_n [m]	H_a [m]	k_{zVol} [rad m^{-1}]

T2013A	2013-05-06	105 / 15	Left	HH	40.9	107.4	-65.6	0.111
T2013B	2013-05-22	198 / 14	Left	HH	38.6	106.5	-61.2	0.121
T2014A	2014-05-09	14 / 7	Left	HH	37.5	145.8	-42.9	0.173
T2014B	2014-06-12	233 / 35	Left	HH	40.8	123.5	-56.6	0.128
T2016	2016-12-10	18 / 2	Right	HH & VV	21.6	50.0	-67.3	0.120
T2018	2018-01-10	18 / 2	Right	HH & VV	22.1	30.2	-112.0	0.072

2.2 Topographic data from optical satellite sensors

Topographic data from the ICESat and ICESat-2 missions and the Reference Elevation Model of Antarctica (REMA), derived from very high resolution optical stereo images (Howat et al., 2019), are available as reference for estimating the elevation bias in the InSAR DEMs. The study area is covered by several tracks of the ICESat and ICESat-2 altimeters. Elevation data were acquired by ICESat during several campaigns between April 2003 and October 2009. We use GLAH12 GLAS/ICESat L2 Global Antarctic and Greenland Ice Sheet Altimetry Data (HDF5), Release 34 (Zwally et al., 2014). This product provides geolocated and time tagged surface elevation estimates, referenced to the TOPEX/Poseidon ellipsoid, corrected for atmospheric delays and tides. The laser footprint size is 60 m to 70 m, the distance between the footprint centres is approximately 170 m. The analysis of repeat-track data allows the detection of the surface elevation change after correcting for elevation differences caused by horizontal shifts of individual footprints. A main cause for the height error of ICESat footprints is the uncertainty in beam pointing, causing slope-induced errors (Brenner et al., 2007; Zwally et al., 2011). ~~Co-located ICESat footprints of 18 campaigns on level terrain in East Antarctica show intercampaign elevation biases between -3.6 cm and +14.7 cm, confirming the high temporal stability (Hofton et al., 2013).~~

Regarding ICESat-2 we use ATLAS/ICESat-2 L3A Land Ice Height, Version 2, Land Ice Along-Track Height Product (ATL06), from the time span 2018-10-14 to 2019-09-01. This data set provides geolocated land-ice surface heights above the WGS 84 ellipsoid, ITRF2014 reference frame, and ancillary parameters including error estimates and quality flags (Smith et al., 2019a). ATL06 heights represent the mean surface height averaged along 40 m segments of ground track, 20 m apart, for each of the six beams of the Advanced Topographic Laser Altimeter System (ATLAS) instrument~~ on board the ICESat-2 observatory~~. The land-ice height is defined as estimated surface height of the segment centre for each reference point~~, using median-based statistics~~ (Smith et al., 2019b).

For spatially detailed comparisons of elevation we use the REMA DEM Tile Nr. 32-19 with 8 m posting, covering Union Glacier (Howat et al., 2019). The dates of the image acquisitions for this tile range from January 2014 to December 2015. The absolute height is based on vertical registration to CryoSat-2 altimetry data, acquired in SARIn mode. In order to account for the CryoSat signal penetration a uniform value of 0.39 m was added to the CryoSat-2-registered heights ~~over the Union Glacier region~~over this tile, regardless of the surface type (Howat et al., 2019). This needs to be taken into account for using the REMA data as elevation reference because the study area includes bare ground, ice surfaces, and snow and firn with different structural properties affecting radar signal penetration. The vertical error estimates for REMA in the region of interest range from 1.0 m to 1.4 m. The error value of each pixel is the standard error from the residuals of the registration to altimetry (Howat et al., 2019). The error due to the use of the bulk Cryosat-2 based penetration correction is not included in this error estimate.

2.3 Snow pit measurements

For the snow pit measurements, made in December 2016,~~s~~ we selected sites covered by ICESat footprints that show different values of coherence and backscatter intensity in TDM data. Backscatter properties of dry snow and firn are controlled by snow microstructure which is also a main factor for X-band radar signal penetration. In the study region the impact of melt for ~~the~~ snow metamorphism is marginal. We detected evidence for melt events in two of the five snow pits: a thin ice crust in 1.1 m depth ~~at P5~~in pit 5 and two thin ice crusts along with one ice layer of 4 cm thickness ~~at P1~~in pit 1. The temperature record from March 2010 to February 2014 at the meteorological station near the runway shows a mean annual air temperature of -21.1 °C and mean monthly temperatures of -8.6 °C for December and -9.3 °C for January. During those years a few short events with air temperatures close to the melting point were recorded.

Profiles of snow density, temperature, hardness, grain size and shape are shown in Fig. 2. The pits vary in depth between 1.6 m and 2.3 m. The observed grain size refers to the maximum axis length of prevailing grains (Fierz et al., 2009). Hardness was estimated by the hand test, ranging from very low (R1) to very high (R5) for snow and R6 for ice. The mean density of snow/firn for layers of 0.5 m vertical extent is specified in Table 2. Grain size and hardness show significant differences between the five measurement sites. The size and shape of the snow grains and the sequence and properties of snow/firn layers are arising from accumulation history, exchange processes of radiation, turbulent heat and mass at the snow/air interface, and vapour diffusion in the snow volume. Down to about 2 m depth the temperature gradient metamorphism is the dominating process for grain growth, triggered by seasonal temperature variations (Alley, 1988; Colbeck, 1983). Average temperature gradients in the top metre of the five snow pits were in the order of 10 °C m^{-1}. At lower depth equi-temperature metamorphism takes over as dominant process for grain growth. Differences in the average grain size of the pits can, at least partly, be attributed to the snow age following from different accumulation rates. Estimates on accumulation rates are based on stake measurements (Rivera et al., 2014), the ice core between pit 2 and pit 3 (Hoffmann et al., 2020), and the summer melt crust in pit 5. Courville et al. (2007) studied the microstructure of snow and firn in a megadune region in East Antarctica. They show that local differences in grain size, thermal conductivity, and permeability are related to spatial accumulation variability in which already relatively small differences in the accumulation rate due to wind redistribution cause significant differences of physical snow properties.

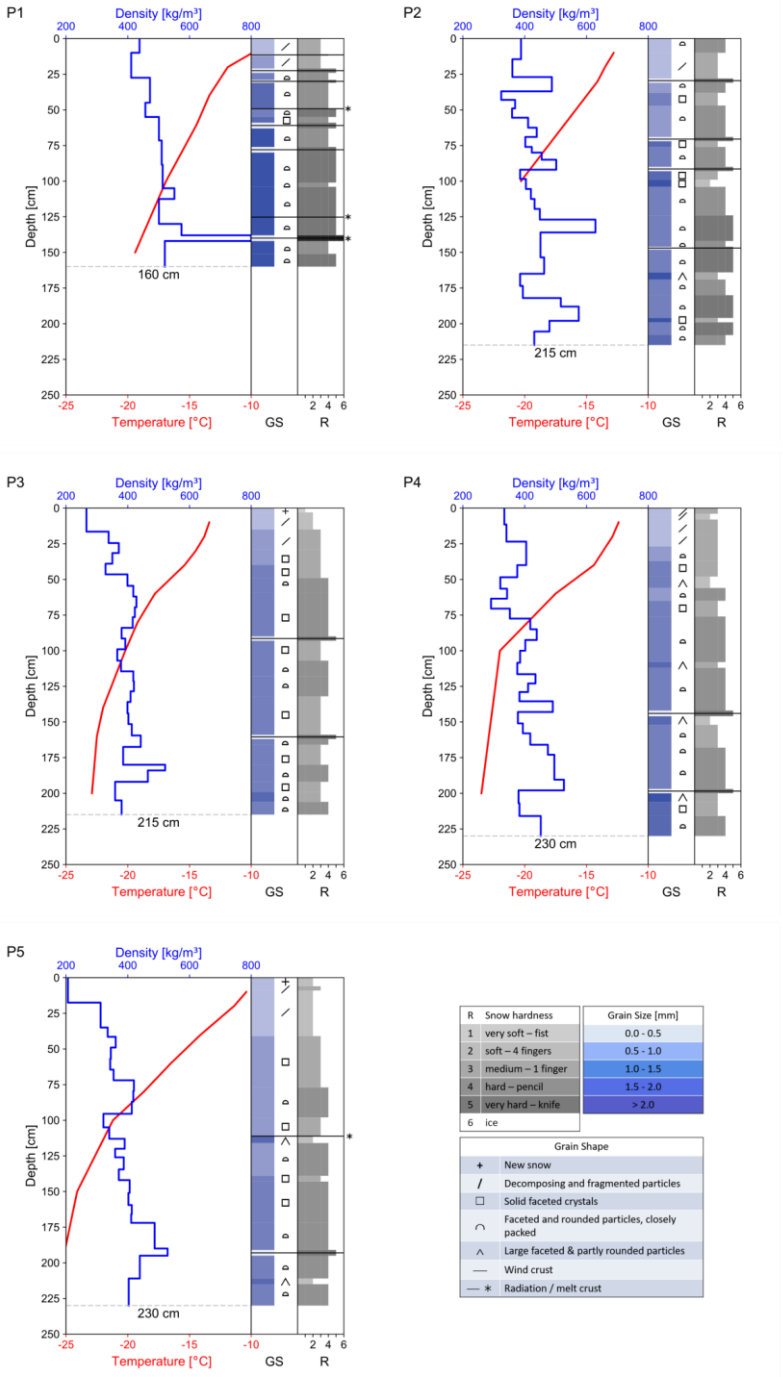
P1
Density [kg/m³]
200 400 600 800
Depth [cm]
0 25 50 75 100 125 150 175 200 225 250
160 cm
-25 -20 -15 -10
Temperature [°C]
GS
2 4 6
R
P2
Density [kg/m³]
215 cm
P3
Density [kg/m³]
215 cm
P4
Density [kg/m³]
230 cm
P5
Density [kg/m³]
230 cm
R Snow hardness
1 very soft – fist
2 soft – 4 fingers
3 medium – 1 finger
4 hard – pencil
5 very hard – knife
6 ice
Grain Size [mm]
0.0 - 0.5
0.5 - 1.0
1.0 - 1.5
1.5 - 2.0
> 2.0
Grain Shape
+ New snow
/ Decomposing and fragmented particles
□ Solid faceted crystals
∩ Faceted and rounded particles, closely packed
∧ Large faceted & partly rounded particles
— Wind crust
— * Radiation / melt crust

Figure 2. Vertical profiles of snow temperature, density, grain size (GS), grain shape and hand hardness (R) for snow pits P1 to P5 on Union Glacier, December 2016. The grain size refers to the maximum axis length of the prevailing snow grains.

Table 2. Mean density of snow/firn for layers of 0.5 m vertical extent of snow pits P1 to P5 on Union Glacier. The snow pit altitude refers to the REMA DEM.

	P1	P2	P3	P4	P5
Altitude [m]	756.8	690.1	674.1	656.0	1133.3
Depth	Snow density [kg m^{-3}]				
0 to 0.5 m	443	390	323	366	286
0.5 to 1.0 m	499	422	408	369	372
1.0 to 1.5 m	548	471	399	408	371
1.5 to 2.0 m		467	419	472	451

Snow pit 1 exhibits the largest grains, the highest snow density, thin ice layers and several wind crusts. Accumulation data are not available, but from the closeness to the BIA it can be concluded that the mean accumulation rate is well below the accumulation rate near the ALE camp. Due to the high exposure to katabatic winds the stratification does not allow ~~a clear~~an identification of annual accumulation layers. In some years sublimation and wind erosion may result in negative mass balance. The higher hardness values compared to the other sites can be attributed to more frequent exposure to high wind speeds, the erosion and deposition of blowing snow and greater age due to low accumulation. Two thin ice crusts (5 mm thickness) at 0.49 m and 1.25 m depth are possibly tracing back to radiation penetration causing melt below the frozen surface (Colbeck, 1989). An ice layer of 4 cm thickness between 1.38 and 1.42 m depth, with air bubbles of up to 2 mm size, indicates an intensive melt event.

P2 is the snow pit with the highest average snow density next to P1. It is located half-way between the runway and the ALE camp, more exposed to katabatic winds than the camp so that the average accumulation rate should be lower than at P3 and P4. The stratigraphy down to 2 m depth shows four layers of high density with comparatively fine-grained snow, typical for wind packs, and several thin wind crusts. Softer layers with faceted grains show up below wind packs, but a clear assignment to seasonal or annual layers is not possible.

The pits P3 and P4, located in the vicinity of the camp, show lower mean density and less variations of density with depth. P4 is located slightly upstream of stake B10 for which Rivera et al. (2014) report a specific mass balance b_n = 0.17 m w.e. a^{-1} for 2008-2009. Down to the depth of 2.04 m the P4 stratification shows four~~,~~ comparatively thick, hard layers with softer, large-grained snow below. The total snow mass down to 2.04 m amounts to 0.80 m w.e. Assuming that the transitions from hard to soft layers corresponds to late summer horizons and accounting for the lack of two months to cover the full 4-year period implies an annual accumulation rate b_n = 0.21 m w.e. a^{-1}. At P3 the sequence of layers is less distinct. This site is located in 300 m cross-wind distance of the camp and may be affected by local perturbations of snow drift during summer when the camp is set up in full extent.

P5 is located at 1133 m elevation on a flat section of a slanting lateral branch of Driscoll Glacier that extends uphill towards the Pioneer Heights, 400 m in altitude above the confluence with Union Glacier. The site is not exposed to the strong katabatic winds that are blowing along the main branch of Union Glacier. The grain size is smaller and the snow is softer than at the other sites. A melt crust of 3 mm thickness was found in 1.14 m depth, most likely related to a short event with comparatively warm temperatures on 17-18 January 2016. The snow

mass above this crust amounts to 0.38 m w.e. A thin hard layer in 2.11 m depth with a soft, coarse-grained layer below refers probably to the 2015 late–summer horizon. The snow mass between the wind crust in late summer 2015 and the melt crust in January 2016, a period of about 13 months, amounts to 0.41 m w.e. These two accumulation estimates indicate for this site about twice the accumulation rate ~~of~~ on the main glacier near the ALE camp.

3. Interferometric coherence and penetration-related elevation bias

The procedure for estimating the interferometric elevation bias is based on the inversion of the volumetric correlation factor which can be derived from total coherence products (γ_{tot}) generated during InSAR processing. The total interferometric complex correlation coefficient (coherence) of a random medium is made up by the following contributions (Krieger et al., 2007):

$$\gamma_{tot} = \gamma_{therm} \cdot \gamma_{Quant} \cdot \gamma_{Amb} \cdot \gamma_{Rg} \cdot \gamma_{Az} \cdot \gamma_{Vol} \cdot \gamma_{temp} \quad (1)$$

The terms on the right-hand side refer to the interferometric correlation coefficient related to the signal-to-noise ratio (γ_{therm}), quantization (γ_{Quant}), azimuth and range ambiguities (γ_{Amb}), baseline decorrelation (γ_{Rg}), relative shift of the Doppler spectra (γ_{Az}), volumetric decorrelation (γ_{Vol}), and temporal decorrelation (γ_{temp}). Temporal decorrelation is not relevant for SP-InSAR data over ground, including snow and ice ($\gamma_{temp} = 1.0$).

The thermal interferometric correlation component is related to the signal-to-noise ratio (SNR) of the two SAR images by:

$$\gamma_{therm} = 1 \Big/ \sqrt{(1 + SNR_1^{-1})(1 + SNR_2^{-1})} \quad (2)$$

For SP-InSAR the volumetric correlation coefficient can be derived from the total coherence by:

$$\gamma_{Vol} = \frac{\gamma_{tot}}{\gamma_{therm}\,\gamma_{Quant}\,\gamma_{Amb}\,\gamma_{Rg}\,\gamma_{Az}} \cdot \quad (3)$$

The phase noise due to γ_{Amb}, γ_{Quant} and γ_{Az} of advanced SAR systems is small. For TDM SP-InSAR interferograms Krieger et al. (2007) estimate the typical loss in coherence for each of the terms γ_{Amb}, γ_{Quant} and γ_{Az} at < 2%. Baseline decorrelation, γ_{Rg}, is avoided by applying common bandwidth filtering.

Hoen and Zebker (2000) specify a formulation for the correlation factor in a uniform volume with exponential extinction in which the interferometric phase is proportional to the penetration length, d_l:

$$\gamma_{Vol} = 1 \Big/ \sqrt{1 + \left(\frac{p\pi \sqrt{\bar{\varepsilon}}\, d_l\, B_n}{r_0 \lambda \tan\theta_i}\right)^2} = 1 \Big/ \sqrt{1 + \left(\frac{\pi \sqrt{\bar{\varepsilon}}\, d_l \cos\theta_i}{H_a}\right)^2} \quad (4)$$

λ is the radar wavelength, r_0 is the slant range distance, θ_i is the incidence angle at the air/snow interface, B_n is the effective interferometric baseline, ε is the dielectric permittivity. p = 1 is valid for the combination of one monostatic and one bi-static SAR image forming an interferogram, p = 2 for the combination of two monostatic images. H_a is the height of ambiguity in free space:

$$H_a = \frac{\lambda\, r_0 \sin\theta_i}{p\, B_n} \quad (5)$$

According to the 1st order radiative transfer approach the one-way power penetration length d_l [m], where the intensity of the signal is attenuated to 1/e of the incident signal, is given by

$$d_l = \frac{1}{k_e} = \frac{1}{k_s + k_a} \quad (6)$$

where k_a and k_s [m^{-1}] are the absorption and the scattering coefficients. The one-way power penetration depth, d_p, referring to vertical direction is obtained by accounting for the refraction angle θ_r:

$$d_p = d_l \cos\theta_r \,. \quad (7)$$

The vertical interferometric wavenumber, k_z [rad m^{-1}], relates the phase of the interferometric correlation to the geometric configuration of the interferometer, providing phase (φ) to height conversion:

$$k_z = \frac{\partial\varphi}{\partial z} = \frac{2\pi}{H_a} \quad (8)$$

The wavenumber in a lossy volume accounts for the change in the propagation constant and refraction (Lei at al., 2016), yielding the following formulation for the height of ambiguity in the volume:

$$H_{aVol} = \frac{2\pi}{k_{zVol}} \,,\ where\ k_{zVol} = k_z \sqrt{\bar{\varepsilon}}\, \frac{cos\ \theta_i}{cos\ \theta_r} = \quad (9)$$

For dry snow and ice the absorption losses are very small so that the real part of the permittivity can be used (Mätzler, 1996). In Table 1 the values for H_a and for k_{zVol} (assuming a snow density of 400 kg m^{-3}) are specified for the TDM scenes.

Dall (2007) shows that the penetration-related elevation bias, h_b, is approximately equal to the two-way power penetration depth, d_{p2}, if the latter is small compared to H_{aVol}. For large relative penetration depths (d_{p2}/H_{aVol}) the elevation bias approaches one quarter of the ambiguity height. Normalizing the coherence by the interferometric phase of the volume surface, so that the coherence is 1 for zero penetration and zero when d_{p2} equals $H_{aVol}/2\pi$, yields the following relation for estimating the elevation bias from the coherence phase (Dall, 2007):

$$h_b \approx {}^{\angle\gamma}/_{k_{zVol}} = {}^{\angle\gamma\ \ |H_{aVol}|}/_{2\pi} \quad (10)$$

As according to this relation the coherence phase, $\angle\gamma$, is uniquely defined by the coherence magnitude, the following formulation can be used for estimating the elevation bias:

$$h_b \approx -\left|\frac{H_{aVol}}{2\pi}\right| arctan\left(\sqrt{|\gamma_{Vol}|^{-2} - 1}\right) \quad (11)$$

We apply this equation for estimating the elevation bias from the observed coherence, using the magnitude of the volumetric InSAR correlation factor as input. According to this formulation the actual InSAR elevation bias becomes progressively smaller than d_{p2} with increasing relative penetration (d_{p2}/H_{aVol}).

This approach is based on the assumption of a uniform volume with exponential extinction whereas dry polar firn is a density stratified medium featuring distinct differences of scattering and extinction properties between individual layers, as well as depth-dependent changes. However, for inverting the observed interferometric coherence in terms of the elevation bias the assumption of a simple model is needed for describing the vertical backscatter and extinction properties. We tested the applicability of the uniform volume approach for describing the observed backscatter intensity, performing forward computations with a multi-layer radiative transfer model (see Appendix).

4. Analysis of backscatter signatures, coherence and elevation bias

In this section we show the spatial pattern of backscatter intensity and coherence in the study area and relations of these parameters to the elevation bias inferred from optical sensor data. We start with an account on topographic reference data and the procedures applied for vertical co-registration, a critical step for estimating the penetration-related elevation bias.

4.1 Topographic reference and vertical co-registration

The precise vertical co-registration on surfaces that are not subject to radar signal penetration is essential for obtaining reliable estimates on the interferometric elevation bias. If the data to be co-registered are lacking temporal coincidence, checks on the temporal stability of the surfaces are needed. These topics are addressed below.

4.1.1 Notations for elevation differences

The apparent glacier surface in an InSAR DEM refers to the position of the scattering phase centre in the snow and firn volume. The elevation bias, h_b, is the difference between the apparent elevation derived by means of the InSAR method, h_{insar}, and the true surface elevation, h_s:

$$h_b = h_{insar} - h_s \,. \qquad (12)$$

For the elevation bias estimate derived from the volumetric coherence we use the notation h_{bInv}. ~~For obtaining reliable estimates of the elevation differences between DEMs from different sources precise vertical co-registration on stable surfaces is needed (Nuth and Kääb, 2011).~~ For studying the penetration-related elevation bias we co-register the TDM DEMs on surfaces devoid of penetration with elevation data of optical sensors. On these surfaces the raw TDM DEMs show vertical offsets up to ~~some~~ a few metres because for these data an absolute height calibration is not performed routinely. We use the notation Δh for the elevation difference between optical data and the un-registered TDM DEMs on surface~~s~~ scattering targets:

$$\Delta h = h_{optical} - h_{TDM,unreg} \qquad (~~2~~13)$$

Suitable targets for vertical co-registration in the study area are the BIA and bare ground on an ice-free slope bordering the BIA ("S" in Fig. 1). ~~The slope has a mean inclination of about 16 degrees and contains sections of varying steepness. On slopes horizontal shifts between pixels of topographic data to be co-registered cause slope-dependent elevation biases, in particular if the data are from sensors with different observation geometries and spatial resolution (Nuth and Kääb, 2011). Therefore we use data from moderately inclined slope sections and from the BIA (with a mean inclination of about one degree) for quantifying the vertical offset between TDM and optical elevation data.~~

We use the notation dh for denoting the elevation difference between the TDM DEMs and optical elevation data, vertically co-registered on surface scattering targets:

$$dh = h_{TDM,coreg} - h_{optical} \qquad (~~3~~14)$$

In case of temporal coincidence or stable topography dh corresponds to the interferometric elevation bias. Though the time series of ICESat data indicate temporal stability of surface elevation in the study area, minor errors due to temporal changes in elevation cannot be fully excluded.

3.14.1.2 Temporal stability of surface elevation

Because of the lack in temporal coincidence between the TDM and optical elevation data we checked the temporal variability using ICESat time series. The main section of the BIA was crossed by ICESat repeat tracks on seven dates between May 2004 and November 2009 (Fig. 1). The mean difference in elevation Δh between the ICESat footprints and the corresponding TDMgl cells (mean values of 5 x 5 pixels) is -6.76 m. The standard deviation for the 126 samples of the time series is 0.43 m (Table S1 in the Supplement). The mean Δh values between the individual ICESat tracks on the different dates and TDMgl range from -6.61 m to -6.86 m without any distinct temporal trend, indicating high temporal stability. The stability of surface elevation on the BIA is also confirmed by the GPS time series of Rivera et al. (2014). The Δh value of -6.76 m can mainly be attributed to the bulk penetration correction of thethat is applied for TDMgl DEM products over Antarctica. The ICESat-2 data set for of the BIA includes eight tracks with altogether 345 spots, extending along the eastern and western margins of the BIA which are occasionally covered by snow. The mean elevation difference and standard deviation are: Δh(ICESat-2-TDMgl) = -6.99 m, $\sigma_{\Delta h}$ = 0.38 m.

In order to check the validity of the assumption that the BIA signal arises from surface scattering we derived optical - SAR elevation differences also on the ice-free slope in the vicinity of the BIA. This slope has a mean inclination of about 16 degrees and contains sections of varying steepness. On slopes horizontal shifts between pixels to be co-registered cause slope-dependent elevation biases, in particular for data from sensors with different observation geometries and spatial resolution (Nuth and Kääb, 2011). Therefore we use data from moderately inclined slope sections for quantifying the vertical offsets.On the ice-free slope the variance of Δh is higher than on the BIA. The different footprint sizes and observation geometries of the ICESat and TDM sensors are prone to slope-induced errors for DEM differencing. In order to avoid steep slope sections we excluded for the comparison all cells of 5 x 5 TDM pixels with a standard deviation of elevation larger than 5 m. Under this constraint only 21 ICESat pixels of the whole time series qualify for the comparison on the slope, yielding a mean Δh of -6.91 m and $\sigma_{\Delta h}$ of 0.84 m. The difference of the mean Δh values between the slope and the BIA is below the measurement uncertainty.

Another ICESat time series for checking the temporal behaviour of surface elevation extends across the main glacier near pit 4 where the average elevation bias of TDMgl due to penetration is several metres. The ICESat data set comprises seven closely-spaced tracks acquired between 11 April 2003 and 12 February 2008. The mean value and standard deviation of the elevation difference between ICESat and the TDMgl are on the central section of the glacier are: Δh = 0.09 m, σ_h = 0.40 m (Table S2). The mean Δh values on individual dates range from -0.03 m to 0.21 m without any obvious temporal trend, confirming also the temporal stability of surface elevation. Subtracting the TDMgl offset of -6.76 m yields a dh value of -6.67 m due to signal penetration.

3.24.1.3 Vertical co-registration of the DEMs

The We use of the REMA elevation data as reference in order to enables obtain spatially detailed estimates of the interferometric elevation bias. The mean value and standard deviation of the elevation difference between ICESat and REMA over the BIA are: Δh = -0.33 m, $\sigma_{\Delta h}$ = 0.38 m (Table S1). This value differs by 6 cm from the bulk penetration correction (-0.39 m) that was applied to CryoSat-2 elevation dataover the Union Glacier area in order to obtain the used as absolute height reference for the REMA DEM (Howat et al., 2019). This correction introduces a bias over bare ice where because the actual CryoSat-2 signal over bare ice is dominated by refers to

surface reflectionreturn whereas the correction accounts for penetration in dry snow. The difference between ICESat-2 and REMA on the BIA is: Δh = -0.54 m, $\sigma_{\Delta h}$ = 0.46 m. On the ice-free slope the elevation differences of REMA versus ICESat, ICESat-2 and TDMgl elevation data show high standard deviations. Therefore we use the BIA as reference site for vertical co-registration between the TDM DEMs and REMA.

For cross-comparing the TDM and REMA elevation data we outlined an area of 5 km^2 extent in the central section of the BIA that is crossed by the ICESat tracks, avoiding BIA sections that are occasionally covered by snow. The mean elevation difference Δh between REMA and TDMgl is -6.37 m, the standard deviation at 8 m x 8 m pixel size is 0.62 m. We use the value of -6.37 m for vertical co-registration of the TDMgl DEM. Data of tThe same polygon are is used for vertical co-registration of the other TDM DEMs which as un-registered DEMs show vertical shifts vs. REMA of 2 m to 3 m.

3. Vertical backscatter distribution and volumetric coherence

For inverting the observed interferometric coherence in terms of the elevation bias the pre-setting of a vertical profile for scattering in the snow/firn volume is required because it is not possible to derive the penetration properties of individual layers. We tested the applicability of the uniform volume approach for describing the observed backscatter intensity and show the resulting relation between the volumetric coherence and the interferometric elevation bias.

3.1 Representation of the vertical backscatter profile

Common approaches for relating the penetration depth, d_p, in a frozen snow/firn medium to the observed coherence are based on the assumption of exponential extinction in a uniform volume (Hoen and Zebker, 2000; Dall, 2007; Fischer et al., 2020). The power received from depth z below the surface in a homogeneous lossy medium is described by an exponential function:

$$P_r(z) = P_{tot}\, exp\left[\frac{2\,z\,k_e}{\cos\theta_r}\right] = P_{tot}\, exp\left[\frac{2\,z}{d_p}\right] \quad (4)$$

P_{tot} is the total backscattered power. P_r is the backscattered power from depth z that is attenuated due to absorption and scattering in the layers above. In the radiative transfer (RT) approach for single scattering the extinction coefficient, k_e, accounts for absorption and scattering losses:

$$k_e = k_a + k_s \quad (5)$$

where k_a and k_s [m^{-1}] are the absorption and the scattering coefficients per unit volume. In a uniform volume the one-way power penetration length d_t [m], where the intensity of the signal is attenuated to 37% of the incident signal, is given by

$$d_t = \frac{1}{k_e} = \frac{1}{k_s + k_a} \quad (6)$$

The one-way power penetration depth referring to vertical direction is obtained by accounting for the refraction angle θ_r:

$$d_p = d_t \cos\theta_r\,. \quad (7)$$

If the elevation bias is much smaller than the height of ambiguity the 2-way power penetration depth, d_{p2}, can be used as reference for the location of the scattering phase centre and as estimate for the interferometric elevation bias (Dall, 2007).

The approach described in Eq. 4 implies constant scattering and extinction coefficients. Actual snow/firn volumes exhibit vertical variations in scattering properties related to layers of different microstructure and density and show a general trend of densification with depth (Fig. 2). In order to check the suitability of the exponential function for inferring the penetration bias from the observed coherence we performed backscatter simulations using the multilayer Snow Microwave Radiative Transfer (SMRT) thermal emission and backscatter model of Picard et al. (2018). The SMRT offers the choice of different electromagnetic and microstructure models for computing the scattering and absorption coefficients and the scattering phase function in a given layer. We apply the sticky hard sphere (SHS) model for characterizing the microstructure and the improved Born approximation (IBA) for computing volume scattering and absorption.

Input parameters for describing the microstructure of each layer with the SHS model are the snow density, the temperature, the diameter of the prevailing snow grains and the stickiness. Closely packed ice particles have a tendency to form clusters and bonds. The stickiness parameter accounts for sintering and clustering of snow grains, forming aggregates that are larger than individual grains. The collective scattering and wave interaction effects of the aggregates result in increased scattering compared to individual grains and show a different phase function with more forward scattering. Löwe and Picard (2015) found stickiness to be an essential parameter when modelling snow as a sphere assembly. They show that the stickiness parameter can be objectively estimated from micro-tomography images. However, objective methods deriving the stickiness parameter from field observations are still pending.

Whereas the stickiness parameter accounts for increased scattering due to sintering, the close packing of particles introduces near field interactions causing reduced scattering. Compared to the assumption of independent scattering elements the scattering in a dense medium decreases with increasing volume fraction of the scatterers larger than about 0.2. Dense Medium Radiative Transfer (DMRT) models, including the IBA, account for dense media effects. We performed test runs with the DMRT model with the Quasi-Crystalline Approximation (QCA) of Mie Scattering (DMRT-QMS) of Tsang et al. (2007) and Chang et al. (2014), showing similar results as the IBA-SHS approach.

For the backscatter simulations of the snow pit sites we accounted for 25 layers with different physical properties. Down to the bottom of the snow pits the grain size and density data are based on the field measurements. The snow density below is adopted from the density profile of the firn core GUPA-1 of Hoffmann et al. (2020), located near P3. For grain size we use the maximum axis length of the prevailing snow grains in each snow layer and assume a moderate increase of grain size with depth below 2 m. This assumption takes into account observations of microstructure in snow pit and firn core samples down to 16 m depth on the West Antarctic Plateau showing significant increase of the mean grain intercept length in the top 2 metres whereas below the increase with depth is weak (Rick and Albert, 2004).

In the SHS model the stickiness parameter, τ, accounts for the degree of bonding between spherical particles. $\tau = 0$ corresponds to infinite stickiness and $\tau = \infty$ to the nonsticky case (Tsang et al., 2013). Typical τ values for computing X-band backscatter range from $\tau = 0.1$ for coarse metamorphic snow to $\tau = 0.5$ for fine-grained snow.

The computed scattering coefficient, k_s, of rounded grains with $\tau = 0.5$ is only slightly larger than then nonsticky case, whereas with $\tau = 0.1$ the scattering coefficient is larger by about one order of magnitude. DMRT-QMS backscatter simulations using τ-values between 0.12 and 0.35 for snow layers of different metamorphic state show good results compared to the measured σ° of seasonal snowpacks in northern Finland (Chang et al., 2014). For comparatively shallow metamorphic snow in Colorado $\tau = 0.1$ is used for matching observations and measurements (Tsang et al., 2013). We chose τ-values in order to match the computed and observed TDM backscatter coefficients and the 2-way power penetration depth deduced from the height difference (dh) between the TDM DEMs and the REMA. The τ-values range from $\tau = 0.1$ for layers with large grains and clusters to $\tau = 0.2$ for near surface layers.

Fig. 3 shows X-band HH-polarized backscatter simulation for 40° incidence angle referring to snow/firn properties of Pit 2 and Pit 4. Pit 2 is located 4 km downstream of the BIA in an area of high wind exposure, exhibiting coarse-grained, clustered snow and distinct differences in density between individual layers. Pit 4 is located in a zone of reduced wind force and higher accumulation rate, featuring smaller average grain size and less variations of density with depth. The computed backscatter coefficient σ°(HH) is -7.96 dB for Pit 2 and -11.81 dB for Pit 4. Both values differ by less than 0.3 dB from the mean σ° of the 2013 and 2014 TDM scenes (Table S3). Based on the computed vertical backscatter profile the 2-way power penetration depth amounts to 4.72 m at Pit 2 and 7.25 m at Pit 4, close to the mean differences dh of the respective TDM 2013/2014 and REMA elevations (Table S4). The computed one-way penetration length at Pit 2 is 10.85 m, close to X-band values (10.4 m) measured on the East Antarctic Plateau (Rott et al., 1993).

The contributions of the individual layers to the total observed power vary with the scattering properties related to the microstructure. There is a general decrease with depth due to the attenuation in the layers above and due to the depth-dependent firn compaction (Figs. 3a and 3c). Layers with coarse grains and grain clusters show higher backscatter coefficients but are thinner than compact layers of higher density such as wind slabs. The variations between individual layers with different scattering properties are smoothed out in the depth-dependent function of the total backscatter power (Figs. 3b and 3d). In order to check the applicability of the exponential loss function we computed the depth dependence of the power contributions by means of Eq. 4, adjusted to the power penetration depth of the multilayer model. The exponential curves are describing the average shape of the multilayer depth dependence of losses quite well. However, there is a minor shift in the top metres due to the overestimation of losses in the near-surface layer with smaller grain size.

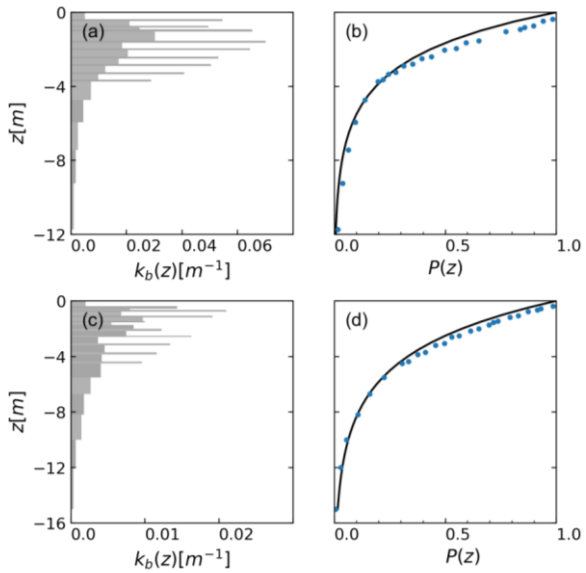

Figure 3. Simulations of X-band HH-polarized backscatter of a dry snow/firn volume at 40 deg. incidence angle. Input parameters refer to Union Glacier Pit 2 (a, b) and Pit 4 (c, d). (a) and (c): Backscatter contribution of individual layers per unit volume attenuated due to propagation through the layers above. (b) and (d): Normalized contributions to total backscattered power in dependence of depth. Symbols: contributions of individual layers. Curve: Model for exponential extinction.

The DMRT simulations for $\theta_i = 40°$, using the observed vertical profiles of grain size and the estimated stickiness, are matching the mean $\sigma°$ values for the 2013 and 2014 TDM data. However, using the same grain size and stickiness values for computing the backscatter at lower incidence angles yields an underestimation of $\sigma°$. The mean $\sigma°_{HH}$ of the TDM 2013 and 2014 data is -7.66 dB at Pit 2 and -11.96 dB at Pit 4. Using the same grain size and τ values for computing $\sigma°$ at $\theta_i = 21.8°$ (the mean θ_i of T2016 and T2018) yields -6.64 dB for Pit 2 and -10.55 dB for Pit 4, whereas the observed $\sigma°_{HH}$ values are -3.75 dB for Pit 2 and -2.85 dB for Pit 4. Agreement between simulated and observed $\sigma°$ can be achieved for the T2016/18 data by setting τ to the value 0.1 for all layers and increasing the grain size of each layer by 30% for Pit 2 and by 80 % for Pit 4, exceeding the observed size. The need for different parameter settings to compute the backscatter coefficients at different incidence angles is an indication for structural anisotropy that is not taken into account by the uniform volume approach. The increased backscatter towards vertical incidence can be attributed to increased contributions of internal interfaces including coherent layer effects (Tan et al., 2017). The angular gradients of the backscatter coefficient show major differences between various glacier sections indicating local differences in the structural anisotropy. Pit 4 is located in a section with a high angular gradient (Fig. S2).

3.2 InSAR coherence in a random medium

The proposed procedure for estimating the interferometric elevation bias is based on the inversion of the volumetric correlation factor which can be derived from total coherence products (γ_{tot}) generated during InSAR

processing. The total interferometric complex correlation coefficient (coherence) of a random medium is made up by the following contributions (Krieger et al., 2007):

$$\gamma_{tot} = \gamma_{therm} \cdot \gamma_{Quant} \cdot \gamma_{Amb} \cdot \gamma_{Rg} \cdot \gamma_{Az} \cdot \gamma_{Vol} \cdot \gamma_{temp} \quad (8)$$

The terms on the right-hand side refer to the interferometric correlation coefficient related to the signal-to-noise ratio (γ_{therm}), quantization (γ_{Quant}), azimuth and range ambiguities (γ_{Amb}), baseline decorrelation (γ_{Rg}), relative shift of the Doppler spectra (γ_{Az}), volumetric decorrelation (γ_{Vol}), and temporal decorrelation (γ_{temp}). Temporal decorrelation is not relevant for SP-InSAR data over ground, including snow and ice ($\gamma_{temp} = 1.0$).

The thermal interferometric correlation component is related to the signal-to-noise ratio (SNR) of the two SAR images by:

$$\gamma_{therm} = \frac{1}{\sqrt{(1 + SNR_1^{-1})(1 + SNR_2^{-1})}} \quad (9)$$

For SP-InSAR the volumetric correlation coefficient can be derived from the total coherence by:

$$\gamma_{Vol} = \frac{\gamma_{tot}}{\gamma_{therm}\gamma_{Quant}\gamma_{Amb}\gamma_{Rg}\gamma_{Az}} . \quad (10)$$

The phase noise due to γ_{Amb}, γ_{Quant} and γ_{Az} of advanced SAR systems is small. For TDM SP-InSAR interferograms Krieger et al. (2007) estimate the typical loss in coherence for each of the terms γ_{Amb}, γ_{Quant} and γ_{Az} at < 2%. Baseline decorrelation, γ_{Rg}, is avoided by applying common bandwidth filtering.

The interferometric vertical wavenumber, k_z [rad m^{-1}], relates the phase of interferometric correlation to the geometric configuration of the interferometer, providing phase (φ) to height conversion:

$$k_z = \frac{\partial\varphi}{\partial z} = \frac{2\pi}{H_a} \quad (11)$$

H_a is the height of ambiguity in free space:

$$H_a = \frac{\lambda r_0 \sin\theta_t}{p B_\pi} \quad (12)$$

λ is the radar wavelength, r_0 is the slant range distance, θ_i is the incidence angle at the air/snow interface and B_a is the effective interferometric baseline. p = 1 is valid for the combination of one monostatic and one bi-static SAR image forming an interferogram, p = 2 for the combination of two monostatic images.

The wavenumber in a lossy volume accounts for the change in the propagation constant and refraction (Lei at al., 2016):

$$k_{zVol} = k_z \sqrt{\bar{\epsilon}} \frac{\cos\theta_t}{\cos\theta_r} = \frac{2\pi}{H_{aVol}} \quad (13)$$

ϵ is the dielectric permittivity, θ_r is the refraction angle and H_{aVol} is the height of ambiguity in the volume. For dry snow and ice the absorption losses are very small so that the real part of the permittivity can be used (Mätzler, 1996). In Table 1 the values of H_a (in vacuum) and k_{zVol} are specified for the TDM scenes. We assume a snow density of 400 kg m^{-3} for computing ϵ.

By applying an exponential loss function as specified in Eq. 4, Dall (2007) derived the following formulation for the complex coherence of a homogeneous infinitely deep scattering medium:

~~$\gamma_{Vol} = \frac{1}{1+j2\pi d_{pz}/H_{aVol}}$ (14)~~

~~Normalizing the coherence by the interferometric phase of the volume surface, so that the coherence is 1 for zero penetration and zero when the two-way penetration depth equals $H_{aVol}/2\pi$, yields the following relation for estimating the elevation bias from the coherence phase (Dall, 2007):~~

~~$h_b \approx \angle\gamma / k_{zVol} = \angle\gamma \, |H_{aVol}| / 2\pi$ (15)~~

~~As the coherence phase in a uniform volume is uniquely defined by the coherence magnitude, the following formulation can be used for estimating the elevation bias in a uniform medium:~~

~~$h_b \approx -\left|\frac{H_{aVol}}{2\pi}\right| arctan\left(\sqrt{|\gamma_{Vol}|^{-2} - 1}\right)$ (16)~~

~~We apply this equation for estimating the elevation bias from the observed coherence, using the magnitude of the volumetric InSAR correlation factor as input. According to this formulation the actual InSAR elevation bias becomes progressively smaller than the two-way penetration depth with increasing relative penetration (d_{p2}/H_{aVol}) and approaches one quarter of H_{aVol} for large ratios.~~

~~Hoen and Zebker (2000) specify a formulation for the volume correlation factor in which the interferometric phase is proportional to the penetration depth:~~

~~$\gamma_{Vol} = \frac{1}{\sqrt{1+\left(\frac{p\pi\, d_t\, B_\pi}{r_0 \lambda \tan\theta_t}\right)^2}} = \frac{1}{\sqrt{1+\left(\frac{\pi \sqrt{\varepsilon}\, d_t \cos\theta_t}{H_a}\right)^2}}$ (17)~~

~~This formulation is based on the same approach for the vertical scattering contributions as used for Eq. 14 and provides for small relative penetration similar results for the relation between h_b and γ_{Vol} as Eq. 16. The difference between the two approaches becomes significant if d_{p2}/H_{aVol} exceeds the value of 0.1 (Fig. S3).~~

~~4. Analysis of the backscatter signatures, coherence and elevation bias~~

~~The analysis and discussion on backscatter signatures, coherence and elevation bias is focussing on the snow pit sites, the BIA and the level glacier area excluding the BIA that is covered by the LGA mask the outline of which is shown in Fig. S1 and in Figs. 8 and 9. The LGA mask covers level areas and slopes smaller than 5° inclination and is completely covered by all of the TDM scenes listed in Table 1. The slope constraint reduces impacts of errors in DEM co-registration and effects of different observation geometries such as radar layover and foreshortening.~~

4.2 Spatial pattern of backscatter signals and coherence

Fig. ~~4~~ 3 shows an image of the backscatter cross section (σ°) and Fig. 4 an image of the total normalized coherence, derived from TDM data of 6 May 2013 (scene T2013A)~~, 9 x 9 pixels low pass filtered~~. The outline encloses the level glacier area (LGA) excluding blue ice areas and slopes smaller than 5° inclination, confining the data used for the statistical analysis of signatures and elevation bias in firn areas (Table 3). Major blue ice areas are located in the vicinity of the landing strip, on Schanz Glacier and at the confluence of Driscoll and

Union glaciers. The LGA area is completely covered by each of the TDM scenes listed in Table 1. The slope constraint reduces impacts of errors in optical and SAR DEM co-registration and effects fore-slopes and layover related to different SAR observation geometries.

The spatial pattern of backscatter intensity on the firn areas ~~level sections~~ of the main glacier and its tributaries reflects primarily differences in volume scattering properties and to some extent also the pattern of the elevation bias (Fig. S4 and Sect. 5). Low σ° values on the LGA refer to ~~the BIA and~~ areas of comparatively fine grained snow~~/~~ and firn in the top layers, whereas high values are an indication for large scattering elements. The ~~BIA has~~blue ice areas have a comparatively smooth surface, accounting for low σ° at an incidence angle of 40°. The ~~L~~lowest σ° values ~~are also evident~~show up on tributary glaciers away from the main passage of the katabatic wind. Low σ° is also evident ~~and~~ at locations of increased accumulation rates in the vicinity of the camp. At lower incidence angles σ° is higher throughout and the overall dynamic range of σ° is reduced, as evident in Fig. S1 which shows backscatter and coherence images of 10 December 2016.

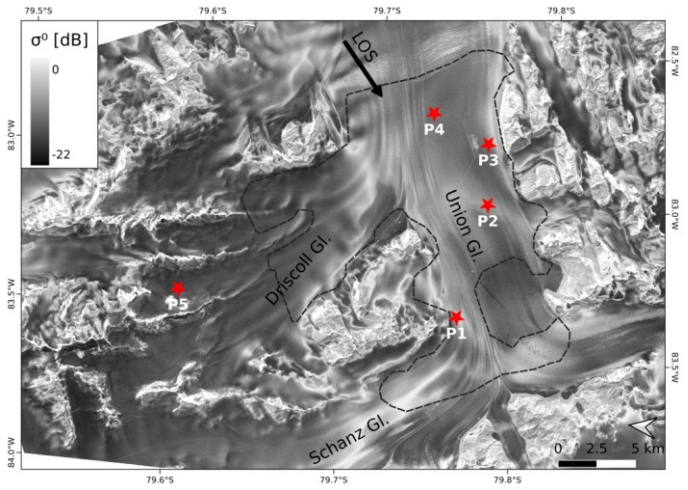

Figure ~~4~~3. Section of TDM backscatter image, HH polarization~~, over Union Glacier~~, 6 May 2013. LOS (line of sight) indicates the radar look direction. The outline encloses the LGA.

The ~~angular gradients~~incidence angle dependence of σ° in the vicinity of the BIA and in crevasse zones ~~are~~ is rather small (Fig. S2). In these areas the differences in σ° between the scenes T2013A (θ_i = 40.9°) and T2016H (θ_i = 21.6°) amount to about ~~2 dB to~~ 3 dB and σ° is high in both scenes. This is an indication for large scattering elements relative to the wavelength ~~such as grain clusters~~. Multiple scattering between individual layers and scattering at rough internal interfaces may also play a role. In the areas with higher accumulation rates the incidence angle dependence ~~angular differences are~~ is larger, reaching values up to 8 dB ~~on the area~~ in the vicinity of pit 4~~orographically left of the camp~~. Large angular gradients of the stratified snow/firn medium can be explained by increased backscatter contributions of internal interfaces towards near-nadir angles. The ~~angular difference~~ pronounced σ° increase ~~of σ°~~towards low incidence angles on the BIA (-13.3 dB in scene T2013A, -5.9 dB in T2016H) is characteristic for backscattering of ~~a~~ slightly rough surfaces (Fung, 1994).

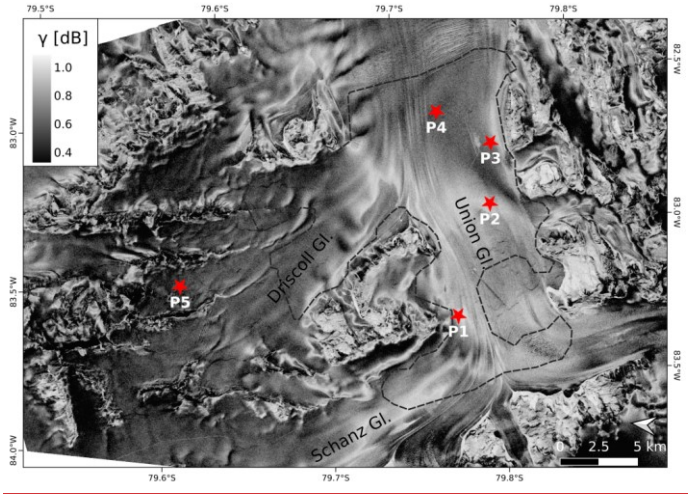

Figure 54. Image of total normalized coherence, γ_{tot}, from the TDM interferogram of 6 May 2013 ~~over Union Glacier~~.

The coherence image of 6 May 2013 (Fig. 45) shows the lowest coherence on glacier sections with large signal penetration. In the T2013 and T2014 (T2013/14) TDM images the coherence of the BIA (mean γ_{tot} = 0.79) is lower than in the surrounding areas because of thermal decorrelation due to the comparatively low SNR. In the surrounding low accumulation areas the σ° values range from -5 dB to -8 dB and the magnitude of γ_{tot} ranges from 0.85 to 0.90. The incidence angle has ~~an~~ also an impact on the relation between coherence and σ°. This is evident by comparing scatterplots of ~~two~~ scenes with different incidence angles (Fig. ~~S4~~S3). The two scenes with 41°, respectively 39° incidence angle ~~2013A~~ show~~s~~ an approximately linear relation between coherence and σ° with two cluster centres corresponding to the surroundings of the BIA ~~and~~ respectively to areas with higher accumulation rates. The scenes with 22° incidence angle (T2016/18~~-~~) ~~scatterplot~~ show reduced dynamic range of coherence and σ°~~s wide scatter with one main cluster~~. The volumetric normalized coherence, derived from the observed total coherence according to Eq. 3, shows the expected variations in dependence of the height of ambiguity and incidence angle(Table 3). The lowest mean coherence value over the LGA is observed for scene T2014A ($|H_a|$ = 42.9 m, γ_{Vol} = 0.656).

4.3 ~~Relation between B~~backscatter signatures, coherence and elevation bias at the snow pit sites

~~We derived t~~The backscatter coefficients, the total and volumetric correlation coefficients and the elevation bias for cells with 90 m diameter centred at the snow pit sites are listed in ~~(~~Tables S3 and S4~~)~~. ~~The azimuth resolution of the single polarization data is 3.3 m and of the dual polarized data 6.6 m. The ground range resolution is 3.34 m at θ_i = 21° and 1.86 m at θ_i = 40°. This yields for the 90 m cells a~~The speckle related uncertainty (standard deviation) for the 90 m cells is~~of~~ 0.13 dB for the single polarized data at θ_i = 40° (~~Case 1~~T2013/14 scenes) and ~~of~~ 0.26 dB for the HH and VV polarized data at θ_i = 22° (~~Case 2~~T2016/18 scenes). The γ-values are based on the coherence pixels whose centre coordinates fit within the corresponding 90 m cell. ~~The absolute and relative radiometric accuracies for the TerraSAR-X stripmap data are estimated at 0.6 dB and 0.3 dB, respectively (Breit~~

et al., 2010). Pit 5 is not covered by the scenes T2016 (10 December 2016) and T2018 (10 January 2018). We derived the data for Pit 5 from two scenes of adjoining tracks with similar height of ambiguity and incidence angle: 7 January 2017 (θ_i = 24.6°, H_a = -70.0 m) and 16 January 2018 (θ_i = 24.7°, H_a = -106.0 m).

The coherence is computed for 11 x 11 pixels estimation windows, adding up to 390 independent samples for Case 1 and 104 independent samples for Case 2. According to the Cramer-Rao bound for coherence estimation the standard deviation for a γ value of 0.5 is 0.03 for Case 1 and 0.05 for Case 2. These uncertainties refer to the impact of random phase noise. The uncertainty decreases towards higher γ values (Bamler and Hartl, 1998). For the snow pit sites we use the average γ values of the coherence pixels whose centre coordinates fit within the 90 m cell. The volumetric normalized coherence, γ_{Vol}, is derived from the observed total coherence according to Eq. 10. The thermal correlation factor is derived from the mean σ° of the snow pit cell and the noise equivalent σ° (NESZ). For deriving γ_{Vol} of the 2013 and 2014 scenes the value 0.96 is used for $\gamma_{Amb} \cdot \gamma_{Quant} \cdot \gamma_{Az} \cdot \gamma_{Rg}$ and -23 dB for NESZ, the corresponding values for the 2016 and 2018 scenes are 0.97 and -24 dB.

Fig. 6 5 shows plots of the volumetric coherence and the backscatter coefficient versus the elevation difference dh between the TDM DEMs and the REMA at the snow pit sites. There is a clear trend of decrease in γ_{Vol} with increasing magnitude of dh. The scene T2014A with the largest vertical wavenumber $|H_a|$ shows the smallest gradient for $dh/d\gamma_{Vol}$ highest sensitivity of γ_{Vol} in respect to dh, and the scene T2018 with the shortest $|H_a|$ shows the lowest sensitivity. with the smallest wavenumber shows the steepest gradient, as expected according to theory. The same behaviour is evident for the whole LGA data sample in which T2014A shows the lowest volumetric coherence and T2018 the highest (Table 3).

Table 3. Mean values over the level glacier area (LGA) for the elevation difference TDM - REMA (dh), the TDM elevation bias by inversion of volumetric coherence (h_{bInv}), the difference between dh and h_{bInv}, the volumetric coherence (γ_{Vol}) and the backscatter coefficient (σ°). R^2 is the coefficient of determination for linear correlation between d_h and h_{bInv}, RMSD is the root mean square difference between d_h and h_{bInv}.

	T2013A	T2013B	T2014A	T2014B	T2016H	T2016V	T2018H	T2018V
dh [m]	-5.97	-5.63	-5.49	-5.10	-4.28	-4.48	-4.78	-4.82
h_{bInv} [m]	-5.80	-5.43	-4.85	-4.78	-4.39	-4.40	-5.17	-5.19
dh -h_{bInv} [m]	-0.17	-0.20	-0.64	-0.32	0.11	-0.08	0.40	0.39
γ_{Vol}	0.791	0.778	0.656	0.808	0.864	0.858	0.927	0.926
σ° [dB]	-9.37	-9.95	-8.21	-9.12	-5.21	-5.36	-4.49	-4.71
R^2	0.57	0.59	0.47	0.49	0.41		0.27	
RMSD [m]	1.88	1.84	2.03	1.56	1.43		1.79	

The incidence angle has also an effect on the elevation bias. For example, the two scenes with almost the same height of ambiguity show different mean dh values of the snow pit sites (Table S4), T2013A: $|H_a|$ = 65.6 m, $\langle dh \rangle$ = 5.93 m; T2016: $|H_a|$ = 67.3m, $\langle dh \rangle$ = 4.35 m. The same behaviour is evident for the mean dh of the LGA (Table 3): $\langle dh \rangle$ = 5.97 m for T2013A and $\langle dh \rangle$ = 4.38 m for T2016. as the differences between the T2013 and T2014 scenes (T2013/14) and the T2016 and T2018 scenes (T2016/18) show. For a uniform volume (Eq. 4) a larger elevation bias $|h_e|$ is expected for T2016/18 due to the steeper propagation path in the snowpack. However, the

~~average dh value at the 5 snow pit sites is -5.34 m for (T2013/14) and -4.47 m for (T2016/18). The same trend is evident for the LGA (Table 3): dh (T2013/14) is -5.55 m, dh (T2016/18) is -4.59 m. This behaviour is an indication for non-isotropic scattering functions with increased scattering contributions towards near-nadir incidence, lifting the position of the scattering phase centre in the volume. It is also in line with the large increase of σ° towards low incidence angles. For estimating the impact of different incidence angles we compare two scenes with (almost) the same vertical wavenumber T2013B (θ_i = 38.6°, k_{zVol} = 0.121) and T2016 (θ_i = 21.6°, k_{zVol} = 0.120): the dh values are -5.63 m (T2013B) and -4.38 m (T2016). Assuming for T2016 the same uniform volume scattering and absorption properties as for T2013B the expected h_b value for T2016 is -6.04 m.~~

Regarding polarization, there are no significant differences between HH and VV polarized data for γ_{Vol} and dh. Whereas the snow pit sites show slightly larger dh at HH polarization, ~~for~~ over the LGA this is the case at VV polarization. The differences in σ° and coherence between HH and VV polarization are also small. The average $\sigma°_{HH}$ of the snow pit sites is 0.28 dB lower than $\sigma°_{VV}$. ~~This is in accordance with DMRT backscatter simulations showing for $\sigma°_{HH}$ values that are lower by 0.3 dB.~~

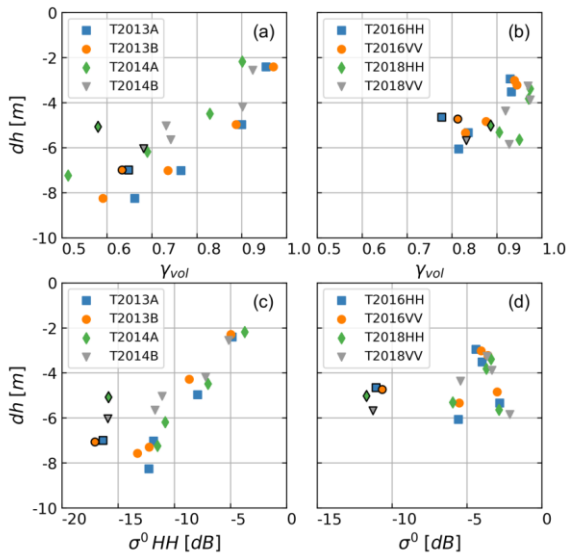

Figure ~~6~~5. Relations between the elevation difference (dh) TDM - REMA and volumetric coherence (a, b), respectively the backscatter coefficient (c, d) for the snow pit sites P1 to P5. The framed points refer to P5.

The plots of dh vs. σ° at the snow pits in Fig. ~~6~~ 5 indicate for the T2013/14 scenes an approximately linear relation for the sites P1 to P4, but the data of P5 (⟨σ°⟩ = -16.3 dB) are shifted by a few dB. The reduced σ° of P5 can be attributed to the smaller grain size and a smoother vertical density profile. The T2016/18 data do not show any ~~obvious clear~~ relation between dh and σ°. P4 with ($\sigma°_{HH}$ -2.8 dB) and P5 ($\sigma°_{HH}$ -11.0 dB) have a similar elevation bias. The same behaviour as for P4, with comparatively deep penetration and high σ° in the T2016/18 data, is evident for an extended area ~~orographically left of the camp~~in its surroundings which shows

high backscatter (mean σ° = -3 dB) and a comparatively large elevation bias in the T2016/18 data (mean dh = -5m). The high σ° at near nadir angles is an indication for increased backscatter at internal interfaces, but it is not clear why this has less impact on volume decorrelation. ~~Reflections between individual layers and interfaces may play a role. The relation between dh and σ° shows also for the full LGA data set a wide spread. The coefficient of determination for linear relations between dh and σ° on the LGA ranges from R^2 = 0.06 for scenes T2016 and T2018 to R^2 = 0.21 for scene T2013B. Part of the spread is caused by speckle related uncertainty and uncertainty in dh, but systematic deviations in sub-regions are also evident, most likely associated with spatial variations in snow/firn microstructure and stratigraphy.~~

5. Estimation of the interferometric elevation bias

Building on the signature analysis reported in Sect. 4, we focus on the use of the volumetric coherence for ~~deriving~~ estimating the interferometric elevation bias by ~~. For~~ inverting γ_{Vol} according to Eq. 11.~~in terms of dh exponential extinction in a uniform volume is assumed. The use of a multi-layer model for inversion is not feasible considering the limited dimension of the available input data.~~ For computing the vertical wavenumber in the volume and the refraction angle we assume a snow density of 400 kg m^{-3}, resulting in ε' = 1.763 (Mätzler, 1996). Fig. ~~7~~ 6 shows plots of the computed elevation bias, h_{bInv}, at the snow pit sites derived from γ_{Vol} vs. the elevation difference dh between the InSAR DEMs and the REMA. In order to check effects of the incidence angle the data derived from the ~~2013 and 2014~~ T2013/14 and from the ~~2016 to 2018~~ T2016/18 scenes are displayed separately. The T2013/14 data show a highly significant linear relation between dh and h_{bInv}, with a coefficient of determination R^2 = 0.86. The root-mean-square difference (RMSD) is 0.74 m, ~~resulting from~~attributed to errors of the computed h_{bInv} and the DEM difference product. The T2016/18 data (mean of HH and VV polarization) show a linear relation with R^2 = 0.59, the RMSD is 0.84 m.

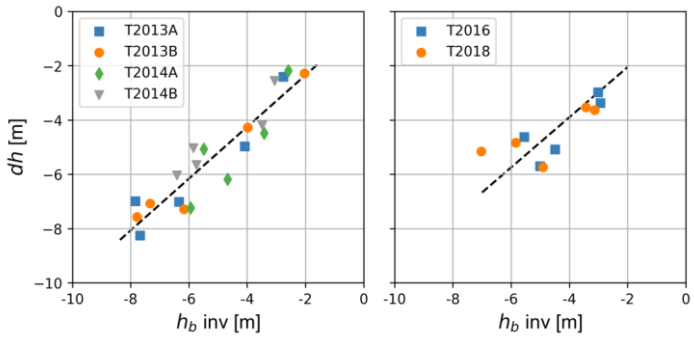

Figure ~~7~~6. Elevation difference (dh) TDM DEM - REMA versus the computed elevation bias, h_{bInv}, derived from the volumetric coherence for the snow pit sites P1 to P5. - - - linear regression line.

Maps of dh and the computed TDM elevation bias are shown in Fig. ~~8~~ 7 for scene T2013B and in Fig. ~~9~~ 8 for scene T2016. These two scenes have almost the same vertical wavenumber but different incidence angles. The differences between HH and VV polarized data of the T2016 and T2018 scenes are insignificant. We use the mean value of the HH and VV based DEMs of the single dates for the ~~statistical~~ comparison in order to reduce the impact of random phase noise. In Table 3 mean numbers over the LGA are specified for dh, h_{bInv} and γ_{Vol}, the

coefficient of determination (R^2) for linear correlation between dh and h_{bInv} and the root-mean square difference (RMSD). The numbers for R^2 and RMSD refer to the maps resampled to 8 m grid size, low-pass filtered over 7 x 7 pixels windows using a Gauss function. The dh value of the TDMgl DEM (dh = 5.61 m) differs only by 0.06 m from the mean dh of the T2013/14 data. The TDMgl DEM~~I~~ is based on several TDM scenes acquired in 2013 and 2014. The dh map for TDMgl vs. REMA shows a similar spatial pattern as dh of the individual DEMs (Fig. ~~S5~~S4).

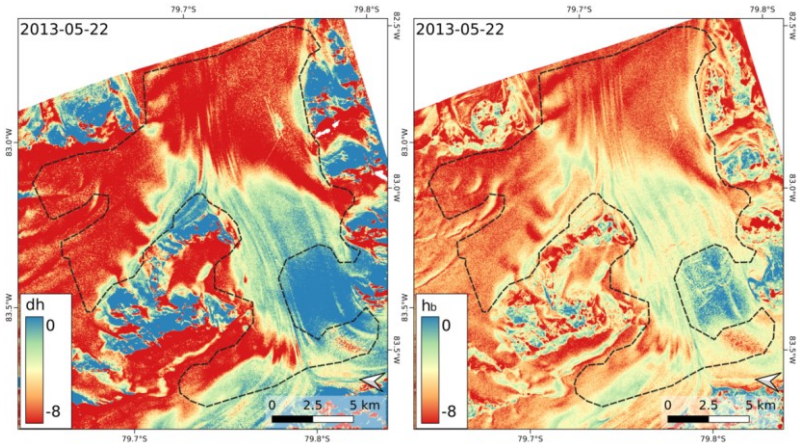

Figure ~~8~~7. Elevation difference (dh) TDM DEM – REMA and elevation bias (h_{bInv}) by inversion of γ_{Vol} for the TDM scene 22 May 2013. The outline encloses the LGA.

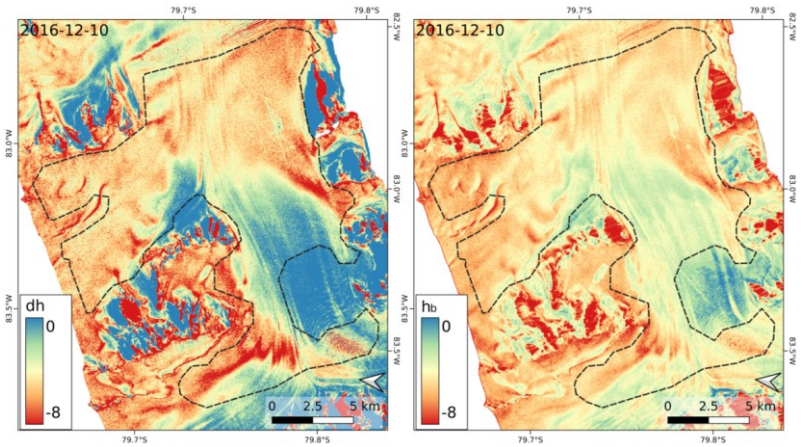

Figure ~~9~~8. Elevation difference (dh) TDM DEM – REMA and elevation bias (h_{bInv}) by inversion of γ_{Vol} for the TDM scene 10 December 2016, based on HH and VV polarized data.

As for the snow pit sites, the mean values over the LGA show distinct differences in dh, h_{bInv} and γ_{Vol} between the data sets with different incidence angle. The magnitudes of the elevation bias of the T2013/14 data (mean dh = -5.55 m, h_{bInv} = -5.22 m) are larger than the corresponding values of the T2016/18 data set (dh = -4.59 m, h_{bInv}

= -4.79 m). As for the snow pit sites, this is opposite to the expectation for a uniform isotropic scattering medium for which $|h_b|$ should be larger for smaller off-nadir angles. ~~The scenes with similar vertical wavenumber show dh = -5.63 m for T2013B and dh = -4.38 m for T2016 whereas the expected value for T2016 is -6.19 m if the same absorption and scattering properties are assumed as for T2013B~~.

The LGA mean values of dh and h_{bInv} show minor differences: -0.32 m for T2013/14 and 0.20 m for T2016/18. The spatial patterns of dh and h_{bInv} are similar, but the mean slope of the 2D distribution deviates from the 1:1 correspondence (Fig. ~~S6~~S5). The magnitude of the computed elevation bias is overestimated over the areas with coarse grained firn and small penetration depth in the surroundings of the BIA and underestimated in areas of higher accumulation rate. These depth dependent deviations can, at least partly, be attributed to the simplified assumption of the uniform volume approach. ~~In the low accumulation areas the large grains, grain clusters and rough interfaces in the top 2 m are efficient scattering sources whereas the high density below causes reduced scattering due to the dense medium effect. In the high accumulation areas the depth of the scattering centre is underestimated because of reduced scattering in surface layers with smaller grains.~~

6. Discussion

A critical issue for inverting interferometric coherence in terms of the InSAR elevation bias is the description of the vertical backscattering profile in the snow volume. A simple model is required, in particular if only single channel backscatter data are available. We apply the model of Dall (2007) in which the vertical backscatter function is defined by the extinction coefficient for a uniform random volume accounting for the combined effect of absorption and scattering. In order to check the suitability of this model for describing the backscattering profile of layered polar firn, we performed backscatter simulations for the snow pit sites with a multilayer radiative transfer (RT) model (see Appendix).

The computed total σ° values at θ_i= 40° are matching the observed total backscatter intensities of the T2013/14 scenes for snow pit sites 2 to 5. The simulated vertical backscatter profiles and the exponential profiles of the UV approach show close agreement for sites 2 to 4. The variations between individual layers, tracing back to accumulation and wind erosion events as well as to seasonal effects, are suppressed in the vertical profile of the cumulative backscatter contributions. At sites 2 to 4 the UV approach shows minor overestimation of the backscatter contributions from the top snow layers due to the assumption of a constant scattering coefficient whereas the actual grain size in the near-surface layers is below average. This effect is more pronounced at pit 5 where the layers with small grains reach down to 1.4 m depth.

On the other hand, the RT simulations at θ_i = 22°, referring to the T2016/18 scenes, yield underestimation of σ° by several dB. For pit 1 the simulated backscatter intensity is underestimated also at θ_i= 40°. The angular differences are most pronounced in the glacier zones with comparatively high accumulation rate (Fig. S2). The increased backscatter towards vertical incidence can be attributed to contributions by internal interfaces related to density stratification and wind crusts, in case of pit 1 also to ice layers. The RT model used for the simulations computes volume scattering for bi-continuous, random structures applying the improved Born Approximation and assumes plane-parallel, homogenous layers (Picard et al., 2018). As matter of fast, in addition to incoherent volume scatter the contributions of rough internal interfaces as well as interlayer interferences play also a role (Tan et al., 2017; Fischer et al., 2019a).

The most likely explanation for the increased backscatter towards near-nadir incidence is the increased scattering at interfaces between layers of different density and wind-packed structures. In particular on the main section of Union Glacier the snow surfaces are wind roughened, showing elongated sastrugi at the metre scale with ripples of centimetres vertical extent. The surface roughness related to wind packing and erosion is also evident in snow pits at interfaces between snow layers and wind crusts. Ashcraft and Long (2006) attribute the backscatter anisotropy, observed in scatterometer data of katabatic wind zones, to the anisotropy in the preferential roughness direction of the snow surface and of internal interfaces. Such behaviour was also observed for density stratified firn on the East Antarctic Plateau and reproduced by simulations with a layered-medium RT model (Rott et al., 1993; West et al., 1996).

Leinss et al. (2016) derived the co-polarized (VV-HH) phase difference (CPD) from TerraSAR-X and ground-based scatterometer data in order to determine the dielectric and structural anisotropy of seasonal snow. The focus of their analysis is on the snow microstructure, showing distinct differences in the structural properties of dry and old snow. The measured CPD is related to differential propagation effects between HH and VV polarized waves in an anisotropic volume, but the sources of the anisotropy are not uniquely defined. In order to check the spatial pattern of the CPD and coherence we computed the complex co-polarized coherence, $\gamma_{HH,VV}$, from data of the T2016 scene (Fig. S6). The CPD is the phase term of $\gamma_{HH,VV}$. Because of the steep incidence angle of the scene the range of CPD values is small. The CPD of the BIA is close to zero, as to be expected for backscatter from a smooth surface. The CPD of the BIA is close to zero, as to be expected for backscatter from a smooth surface. Whereas the spatial pattern of the CPD does not show any clear relation to the backscatter intensity and the elevation bias, the magnitude of the co-polarized coherence $|\gamma_{HHVV}|$, reflects to some degree the spatial pattern of the elevation bias. $|\gamma_{HHVV}|$ is low (0.3 to 0.5) on areas with deep penetration. This can be attributed to volumetric decorrelation due to the non-coherent components of scattering in the volume and at internal interfaces.

Whereas differential propagation effects lead to distinct co-polarization differences in the phase and magnitude of the complex co-polarized coherence, the differences in the interferometric coherence and derived penetration bias between the individual polarizations are insignificant (Table 3). This implies that the vertical backscatter distributions of the co-polarizations channels are similar. Consequently, the data from HH and VV polarization can be combined for estimating the elevation bias, reducing the impact of noise. The differences in $\sigma°$ between HH and VV polarization are also small, as to be expected for low incidence angle data (Fung, 1994). On the average over the LGA $\sigma°_{HH}$ is higher by 0.2 dB compared to $\sigma°_{VV}$ and there is no distinct spatial variability.

According to theory the penetration bias and phase centre depth at a given frequency and polarization change with the baseline and the incidence angle (Dall, 2007). This was verified with airborne data by Fischer et al. (2020), showing that the changes are significant in particular at small volumetric wavenumbers (long baselines). This is evident comparing two scenes with almost the same incidence angle: T2016 (θ_i = 21.6°, k_{zVol} = 0.120) and T2018 (θ_i = 22.1°, k_{zVol} = 0.072). Both the dh and h_{bInv} values indicate deeper penetration for T2018 compared to 2016, amounting on the LGA to 0.42 m, respectively 0.68 m (Table 3).

For a uniform scattering function and absorption deeper penetration is expected for a steeper propagation path (lower incidence angle). This can be checked by comparing two scenes with almost the same vertical wavenumber and different incidence angles: T2013B (θ_i = 38.6°, k_{zVol} = 0.121, dh(LGA) = -5.63 m) and T2016

(θ_i = 21.6°, k_{zVol} = 0.120, dh(LGA) = -4.38 m). However, assuming for T2016 a volume with the same scattering and absorption coefficients as for T2013B, the expected elevation bias for T2016 is -6.04 m. The same behaviour is evident for the mean dh values of the snow pit sites (dh = -5.70 m for T2013B, dh = -4.35 m for T2016). This mismatch points also to increased scattering at internal interfaces at low incidence angles, as concluded from backscatter modelling (see Appendix).

The impact of the incidence angle on the mean difference between the observed dh and the computed h_{bInv} is small. For T2103/14 the mean value for dh - h_{bInv} amounts to -0.33 m, for T2016/18 to 0.20 m (Table 3). This shows that the uniform volume approach, based on the volumetric coherence, delivers reasonable mean penetration corrections. However, biases for deep, respectively shallow penetration, indicate systematic deviations from the UV approach. In the first case the smaller grain size of the top snow layers causes a shift of the scattering phase centre to larger depth compared to exponential extinction. The second case, an overestimation of h_b in wind exposed low accumulation zones, can be attributed to the larger size of the scattering elements and a denser sequence of internal interfaces.

7. Conclusion

In this study we investigated the feasibility for estimating the penetration-related elevation bias of interferometric topographic products over snow and ice by inverting the volumetric coherence. Single-pass across-track SAR interferometry has been widely applied for comprehensive, spatially detailed measurements of glacier and ice sheet topography as the measurements are not impaired by temporal decorrelation of the interferometric signal, variations in atmospheric propagation conditions, cloudiness, and variable illumination. A main concern for the use of InSAR DEMs over glaciers and ice sheets is the correction of the elevation bias. A common approach is the use of laser altimetry data as reference for vertical co-registration (e.g. Abdullahi et al., 2019, Rizzoli et al., 2017a; 2017b; Wessel at al., 2016). However, altimetry data often lack the required temporal coincidence and coverage for comprehensive corrections.

We applied and evaluated the method of Dall (2007) for deriving the elevation bias of dry polar snow and firn by inverting the volumetric coherence of X-band InSAR data of the TanDEM-X mission. This method is based on the assumption of a uniform volume with constant scattering and absorption properties whereas actual snow/firn volume shows depth-dependent changes of the density and the scattering elements, as well as variations at small vertical scale related to stratification. The use of a simple model is required because the inversion of a single parameter does not allow the representation of the complex layered structure of natural snow. The study area, Union Glacier in Antarctica, comprises ice-free surfaces, bare ice and dry snow and firn with different structural properties depending on wind exposure and accumulation, a suitable environment for studying the performance of the inversion algorithm. For the statistical analysis we focus at the level glacier area, including sites of field measurements, in order to minimize the impact of possible errors in SAR image co-registration with optical reference data.

The TanDEM-X data set comprises interferometric pairs with different interferometric baselines, as well as with two distinctly different incidence angle ranges. This enables to study the impact of these parameters on the computed elevation bias. In spite of the simplified representation of the vertical backscatter profile the inversion according to the model of Dall (2007) provides reasonable estimates. The mean values for the computed

elevation bias over the level glacier area range from -4.4 m to -5.8 m, varying with the baseline and incidence angle. The mean differences to the penetration bias estimate based on optical reference data range from 0.40 m to -0.64 m for the different TanDEM scenes. However, there is a trend for overestimation of the elevation bias in areas that are subject to high wind exposure and low accumulation rates and for underestimation in areas with high accumulation rates. In both cases deviations from the uniform volume structure are the main reason. In the first case the dense sequence of horizontal structures related to internal wind crusts, ice layers and density stratification causes increased scattering in the near-surface layers. In the second case the smaller grain size of the top snow layers causes a downward shift of the scattering phase centre compared to the uniform volume approach.

Advancements for the estimation of the InSAR elevation bias can be expected from progress in the representation of snow/firn structural properties in models for radar signal propagation. After all, the derivation of the interferometric elevation bias from volumetric coherence is a promising option which should be carried forward as it delivers spatially detailed information coinciding both in space and time with the topographic products. Fischer et al. (2020) analysed deviations from the uniform volume approach for airborne multi-frequency polarimetric SAR data. They explored sources and interaction mechanisms responsible for these deviations and tested different models for vertical backscatter contributions, concluding that in case of single polarization data the inversion based on the uniform volume model is a preferred approach. Beyond that, Fischer at al. (2019b) demonstrated the added value of multi-baseline polarimetric InSAR data for deriving the depth of dominant scattering layers in polar firn, key information for locating the position of the scattering phase centre within the volume. Consequently, further progress on InSAR signal penetration in layered media can be expected from the use of polarimetric data as well as from multi-baseline and multi-angle observations.

Appendix: Representation of the vertical backscatter profile

In order to assess the suitability of the vertical backscatter distribution of the uniform volume approach we performed backscatter simulations with a multilayer radiative transfer (RT) model. According to the RT theory the normalized radar cross section scattered back from depth z of a random scattering medium and received at the surface can be described by:

$$\sigma^0(z) = T^2(\theta_i)\sigma_v^0(z)\, exp\left\{2\int_z^0 \left[\frac{k_e(z)}{\cos\theta_r}\right] dz\right\} \quad \text{(A1)}$$

T is the transmissivity at the air/snow interface, σ^0_v is the volume scattering coefficient, k_e is the volume extinction coefficient accounting for scattering and absorption losses. θ_i is the incidence angle at the surface, θ_r is the refracted incidence angle; z within the medium is negative. The factor 2 accounts for the two-way travel path in the volume. The uniform volume approach assumes constant scattering and extinction properties (Hoen and Zebker, 2000). The resulting vertical backscatter function, accounting for two-way losses, is given by

$$\sigma^0(z) = \langle\sigma_v^0\rangle\, exp\left(\frac{2\,z\,k_e}{cos\theta_r}\right) = \langle\sigma_v^0\rangle\, exp\left(\frac{2\,z}{d_p}\right) \quad \text{(A2)}$$

$\langle\sigma^0_v\rangle$ is the average normalized volume scattering cross section, d_p is the one-way power penetration depth.

We performed backscatter simulations for the snow pit sites with the multilayer Snow Microwave Radiative Transfer (SMRT) thermal emission and backscatter model of Picard et al. (2018). The SMRT offers a choice of

different electromagnetic and microstructure models for computing the scattering and absorption coefficients and the scattering phase function in a given layer. We used the sticky hard sphere (SHS) model for characterizing the microstructure and the improved Born approximation (IBA) for computing volume scattering and absorption. Input parameters for describing the microstructure of each layer with the SHS model are the snow density, the temperature, the effective grain size and the stickiness. The effective grain size refers to the maximum axis length of the prevailing snow grains in each layer (Fierz et al., 2009). Down to the bottom of the snow pits the grain size and density data are based on the field measurements. The increase of snow density below is adopted from the density profile of the firn core GUPA-1 of Hoffmann et al. (2020). For estimating the increase of grain size with depth below snow pit depth we apply the grain growth model of Linow et al. (2012).

The stickiness parameter, τ, is used in the SHS models to account for sintering and clustering of snow grains, forming aggregates that are larger than individual grains. The collective scattering and wave interaction effects of the aggregates result in increased scattering compared to individual grains and show a different phase function with more forward scattering. Löwe and Picard (2015) found stickiness to be an essential parameter when modelling snow as a sphere assembly. They show that the stickiness parameter can be objectively estimated from micro-tomography images. However, objective methods for deriving the stickiness parameter from field observations are pending. Typical stickiness values for X-band backscatter simulation of coarse-grained metamorphic snow are $\tau = 0.1$, whereas $\tau = 1.0$ is similar to the nonsticky case (Chang et al., 2014). We chose τ-values in order to match the average observed and the computed backscatter coefficients at the individual sites. The τ-values range from $\tau = 0.1$ for layers with large grains and clusters to $\tau = 0.2$ for near surface layers.

Whereas the stickiness parameter accounts for increased scattering due to bonding, the close packing of particles introduces near field interactions causing reduced scattering (Tsang et al., 2013). Compared to the assumption of independent scattering elements the scattering in a dense medium decreases with increasing volume fraction of the scatterers larger than about 0.2. We performed test runs with the dense medium RT model with the Quasi-Crystalline Approximation (QCA) of Mie Scattering (DMRT-QMS) of Tsang et al. (2007) and Chang et al. (2014) using the same stickiness and grain sizes parameters as for the IBA-SHS approach of SMRT. The results of both models are in close agreement and point out that the parameterization of snow microstructure is decisive for snow backscatter simulations.

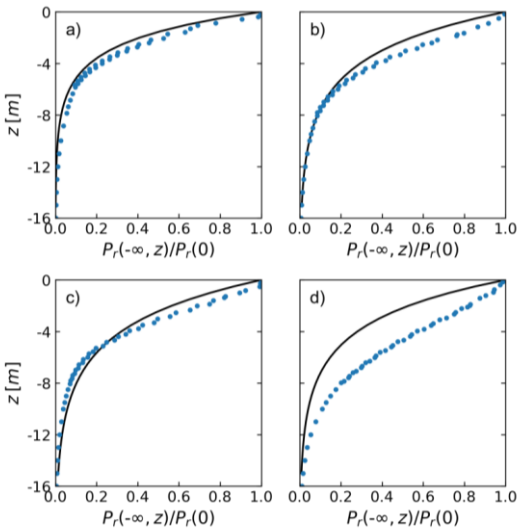

Figure A1. Fraction of X-band HH-polarized power scattered back from the snow/firn volume below the depth z. Points: RT model computations for individual layers. Curve: Model for exponential extinction. Input parameters refer to Union Glacier Pit 2 (a), Pit 3 (b), Pit 4 (c) and Pit 5 (d).

Fig. A1 shows vertical profiles of the power scattered back from the volume below a specific depth as fraction of the total power observed at the surface, both for multilayer RT modelling results and the uniform volume (UV) approach. The RT computations refer to θ_i = 40°, the mean local incidence angle at the snow pit sites of the T2013/14 scenes. The extinction coefficient for the exponential UV function is based on the mean penetration depth which is deduced from the mean elevation difference (dh) between the T2013/14 scenes and the REMA.

Layers with coarse grains and grain clusters show higher backscatter coefficients but are thinner than compact layers of higher density such as wind slabs. The variations between individual layers with different scattering properties are smoothed out in the depth-dependent backscatter function. Consequently, the exponential function is able to reproduce the vertical backscatter profiles quite well. The reduced backscatter contributions from near surface layers shown by the RT model can be attributed to the smaller grain size whereas the UV model assumes constant scattering cross section. This effect yields for pits 2, 3 and 4 only minor differences between the two models. At pit 5 the differences are more pronounced due to the smaller gain size of the top layers related to the higher accumulation rate.

The RT simulations are able to reproduce the observed total backscatter intensity at snow pit sites 2 to 5 for θ_i = 40°. For pit 1 the simulations for θ_i = 40° yield an underestimation of 3 dB, very likely due to neglect of the scattering contributions of ice layers and wind crusts. The RT simulations for θ_i = 22°, corresponding to the T2016/18 incidence angle, show underestimation throughout. For pit 2 to pit 5 the simulations show from 40° to 22° incidence angle an average σ° increase of 1.3 dB, whereas the observed increase is 5.9 dB. Such an angular difference is typical for density-layered firn. Ground-based X-band scatterometer measurements at several sites in the dry snow zone of Dronning Maud Land with accumulation rates between 130 and 260 kg m^{-2} a^{-1} ,

comparable to those on Union Glacier, show from 40° to 20° incidence angle a mean increase of σ° by 6.5 dB (Rott et al., 1993). The strong increase towards low off-nadir angles is an indication for increased scattering at horizontal structures such as rough interfaces between snow layers of different density and wind crust whereas the RT model assumes plane-parallel layered structures.

~~6. Discussion and conclusion~~

~~Single-pass across-track SAR interferometry is an efficient technique for comprehensive, spatially detailed measurements of glacier and ice sheet topography as the measurements are not impaired by temporal decorrelation of the interferometric phase, variations in atmospheric propagation conditions, cloudiness, and variable illumination. However, the penetration of the InSAR signal into snow and ice introduces a bias in the measured elevation. Empirical and model-based approaches have been applied for correcting the elevation bias in InSAR DEMs. A common approach is the use of laser altimetry data as reference for vertical co-registration. However, the altimetry data often lack the required temporal coincidence and spatial coverage. For repeat measurements with the same SP-InSAR sensor and observation geometry the backscatter coefficients and coherence can be used as indicators for stability or changes of snow volume properties and signal penetration. In case of unchanged backscatter and coherence values no correction is required for deriving glacier elevation change (Rott et al., 2018). However, for the majority of applications corrections for penetration are needed, in particular if elevation data from different sensors are used.~~

~~The theoretical and experimental work reported by Hoen and Zebker (2000) and Dall (2007) suggests the use of the volumetric coherence as a key parameter for estimating the InSAR signal penetration. In order to evaluate the suitability of this approach for polar snow and firn we analysed multiple SP-InSAR data of the TanDEM-X mission over Union Glacier. The inversion of a single parameter does not allow the detailed representation of the complex layered structure of natural snow. Therefore we use a simplified model, the uniform volume approach, for describing the scattering and absorption properties. In order to check the suitability of this approach for inferring the InSAR signal propagation in snow and firn volumes with different structural properties we performed simulations with a multi-layer dense medium radiative transfer model. The computations show large variations of the backscatter coefficient between individual layers but the average depth-dependent backscatter contributions can be approximated by an exponential function that reflects the extinction in a uniform medium. However, the model underestimates the increase of backscatter towards low incidence angles. This can be explained by structural anisotropy in which horizontally oriented scattering elements are causing increased backscatter towards near-nadir angles (Nghiem et al., 1993). Measurements of fabric and microstructure in the top 3 m of snow on the East Antarctic plateau show minor structural anisotropy for grain layers that are subject to strong temperature gradients (Calonne et al., 2017). Randomly orientated c-axes are observed in denser layers of rounded grains, whereas a preferential orientation in the horizontal plane shows up in large faceted grain layers. However, such layers are absent in the wind exposed zones of Union Glacier and marginal in other sections, excluding anisotropy of grains as a main explanation for the observed angular backscatter behaviour.~~

~~A most likely explanation is increased forward scattering at internal interfaces and wind-packed structures. In particular on the main section of Union Glacier the snow surfaces are wind roughened, showed elongated sastrugi of metre length with steps and ripples of several centimetres vertical extent. The surface roughness related to wind packing and erosion is also evident in snow pits at interfaces between snow layers and wind~~

crusts. Ashcraft and Long (2006) attribute the backscatter anisotropy, observed in scatterometer data of katabatic wind zones, to the anisotropy in the preferential roughness direction of the snow surface and internal boundaries. Such behaviour was also observed for density stratified firn on the East Antarctic Plateau and reproduced by simulations with a layered-medium RT model (Rott et al., 1993; West et al., 1996).

The observed differences of the elevation bias at different incidence angles are another evidence for structural anisotropy. For a uniform lossy medium larger values of the penetration depth and elevation bias are expected at near nadir angles. However, the 2013/2014 TDM data and 2016/2018 TDM data show the opposite behaviour. As for the observed angular backscatter gradients this can be explained by increased backscatter contributions at internal interfaces at small off-nadir angles.

Constraints of the uniform volume model are also evident in the deviation from an exact 1:1 correspondence between the observed elevation difference dh and the computed elevation bias, h_{bias}. Whereas the mean values of dh and h_{bias} show only minor differences, a trend towards overestimation of the computed penetration is evident for the heavily wind-exposed areas and towards underestimation for areas with reduced impact of wind and deeper signal penetration. In the first case large grains, clusters and wind crusts in the top layers act as strong scattering elements whereas the high density causes a pronounced decrease of scattering with depth. Multi-layer interactions between the internal interfaces may also play a role as observed in tomographic experiments (Fischer et al., 2019a). In the areas with higher accumulation rates the top snow layers show below-average grain size implying reduced scattering. In this case the assumption of uniform extinction properties introduces an underestimation of the computed elevation bias. This effect was also observed in the percolation zone of Greenland by Fischer at al. (2019b) where the assumption of uniform scattering and extinction leads to an underestimation of the phase centre depth due to below-average grain size in the top layer.

In spite of the issues addressed above, the average values of the elevation bias over Union Glacier, derived from volumetric coherence, agree well with the mean elevation difference between the TDM and optical DEMs. The spatial patterns of the simulated and observed elevation bias are also quite similar. As the deviations from the 1:1 correspondence of dh and h_{bias} are not random but related to spatial variations of the snow and firn structure, advancements for the estimation of the InSAR elevation bias can be expected from progress in the representation of snow/firn structural properties in models for radar signal propagation. After all, the derivation of the interferometric elevation bias from volumetric coherence is a promising option which should be carried forward as it delivers spatially detailed information coinciding both in space and time with the topographic product.

Fischer et al. (2020) observed also deviations from the uniform volume approach for deriving the volumetric coherence from airborne multi-frequency polarimetric SAR data. They explored sources and interaction mechanisms responsible for these deviations and tested different models for vertical backscatter contributions, concluding that in case of single polarization data the inversion based on the uniform volume model is a preferred approach. Progress for locating the scattering sources in layered polar firn and estimating the InSAR penetration bias can be expected from the use of polarimetric radar data. Parrella et al. (2016) developed a polarimetric scattering model accounting for structural anisotropy in layered firn. They applied this model to polarimetric L-band SAR data for deriving the shape and orientation of scattering elements in the firn volume. Fischer at al. (2019a) derived the depth of dominant scattering layers in firn from multi-baseline polarimetric interferometric SAR data in different frequency bands, including X-band. Consequently, further progress on

~~InSAR signal penetration in layered media can be expected from the use of polarimetric data as well as from multi-baseline and multi-angle approaches.~~

Data availability. Interferometric satellite products processed for this study will be made available upon publication of the final version of the manuscript at http://cryoportal.enveo.at/.

Supplement. The supplement related to this article is available on-line.

Author contributions. HR conceived the study, performed the field work, was in charge of the data analysis and scientific interpretation and drafted the manuscript. SS, ~~and~~ JW and LL contributed to ~~numerical~~ backscatter analysis and numerical simulations, and to the analysis of topographic data. LK processed and calibrated the interferometric satellite data. All authors contributed to the data interpretation, discussion of the results and revision of the manuscript.

Competing interests. The authors declare that they have no conflict of interest.

Acknowledgements. The TanDEM-X data were made available by DLR through the projects XTI_GLAC6809 and DEM_GLA1059. The ICESat and ICESat-2 laser altimeter data were obtained from the NASA Distributed Active Archive Center, US National Snow and Ice Data Center (NSIDC), Boulder, Colorado. REMA data were downloaded from the U.S. Polar Geospatial Center. Landsat 8 images were downloaded from the United States Geological Survey (USGS) Landsat Archive. HR would like to thank Antarctic Logistics & Expeditions LLC (ALE) for perfect logistic support and for the provision of meteorological data and in particular Nate Opp for his active and knowledgeable support in the field work.

References

Abdullahi, S., Wessel, B., Huber, M., Wendleder, A., Roth, A., and C. Kuenzer, C.: Estimating penetration-related X-Band InSAR elevation bias: A study over the Greenland Ice Sheet, Remote Sens., 11, 2903; doi:10.3390/rs11242903, 2019.

Alley, R. B.: Concerning the deposition and diagenesis of strata in polar firn, J. Glaciol., 34 (118), 283 – 290, 1988.

Ashcraft, I. S., and Long, D. G.: Relating microwave backscatter azimuth modulation to surface properties of the Greenland Ice Sheet, J. Glaciol., 52 (177), 257–266, 2006.

Bamler, R. and Hartl, P.: Synthetic aperture radar interferometry, Inverse Problems, 14, R1 - R54, 1988.

Breit, H., Fritz, T., Balss, U., Lachaise, M., Niedermeier, A., and Vonavka, M.: TerraSAR-X processing and products, IEEE Trans. Geosci. Rem. Sens., 48 (2), 727–740, 2010.

Brenner, A. C., DiMarzio, J. P., and Zwally, H. J.: Precision and accuracy of satellite radar and laser altimeter data over the continental ice sheets, IEEE Trans. Geosc. Rem. Sens., 45(2), 321-331, 2007.

~~Calonne, N., Montagnat, M., Matzl, M., and Schneebeli, M.: The layered evolution of fabric and microstructure of snow at Point Barnola, Central East Antarctica, Earth and Planetary Science Letters 460, 293–301, 2017.~~

Chang W., Tan, S., Lemmetyinen, J., Tsang, L., Xu, X., Li, X., and Yueh, S.: Dense media radiative transfer applied to SnowScat and SnowSAR, IEEE J. Sel. Topics Applied Earth Obs. Rem. Sens., 7, (9), 3811-3825, 2014.

Colbeck, S. C.: Theory of metamorphism of dry snow, J. Geophys. Res., 88(C9), 5475–5482, 1983.

Colbeck, S. C.: Snow-crystal growth with varying surface temperatures and radiation penetration, J. Glaciol., 35 (119), 23-29, 1989.

Courville, Z. R., Albert, M. R., Fahnestock, M. A., Cathles, L. M., and Shuman, C. A.: Impacts of an accumulation hiatus on the physical properties of firn at a low-accumulation polar site, J. Geophys. Res., 112(F2), F02030 (doi: 10.1029/2005JF000429), 2007.

Dall, J.: Elevation bias caused by penetration into uniform volumes, IEEE Trans. Geosc. Rem. Sens., 45(7), 2319–2324, 2007.

Dall, J., Madsen, S. N., Keller, K., and Forsberg, R.: Topography and penetration of the Greenland Ice Sheet measured with airborne SAR interferometry, Geophys. Res. Letters, 28(9), 1703-1706, 2001.

Fierz, C., Armstrong, R.L., Durand, Y., Etchevers, P., Greene, E., McClung, D.M., Nishimura, K., Satyawali, P.K., and Sokratov, S.A.: The International Classification for Seasonal Snow on the Ground, IHP-VII Technical Documents in Hydrology No. 83, IACS Contribution No. 1, UNESCO-IHP, Paris, 2009.

Fischer, G., Papathanassiou, K. P., and Hajnsek, I.: Modeling multifrequency Pol-InSAR data from the percolation zone of the Greenland Ice Sheet, IEEE Trans. Geosc. Rem. Sens., 57 (4), 1963–1976, 2019a.

Fischer, G., Jäger., M., Papathanassiou, K. P., and Hajnsek, I.: Modeling the vertical backscattering distribution in the percolation zone of the Greenland Ice Sheet with SAR tomography, IEEE J. Sel. Topics Applied Earth Obs. Rem. Sens., 12 (11), 4839 – 4405, 2019b.

Fischer, G., Papathanassiou, K. P., and Hajnsek, I.: Modeling and compensation of the penetration bias in InSAR DEMs of ice sheets at different frequencies, IEEE J. Sel. Topics Applied Earth Obs. Rem. Sens., 13, 2698-2707, 2020.

Forsberg, R., Keller, K., Nielsen, C. S., Gundestrup, N., Tscherning, C. C., Madsen, N. S., and Dall, J.: Elevation change measurements of the Greenland Ice Sheet, Earth Planet. Space, 52, 1049-1053, 2000.

Fung, A.K.: Microwave Scattering and Emission Models and Their Applications, Artech House, Boston, London, 1994.

~~Gatelli, F., Monti Guarnieri, A. M., Parizzi, F., Pasquali, P., Prati ,C., and Rocca, F.: The wavenumber shift in SAR interferometry, IEEE Trans. Geosc. Rem. Sens., 32(4), 855-865, 1994.~~

Hoen, E.W., and Zebker, H. A.: Penetration depths inferred from interferometric volume decorrelation observed over the Greenland Ice Sheet, IEEE Trans. Geosc. Rem. Sens., 38(6), 2571-2583, 2000.

Hoen, E.W., and Zebker, H. A.: Correction to: Penetration depths inferred from interferometric volume decorrelation observed over the Greenland Ice Sheet, IEEE Trans. Geosc. Rem. Sens., 39(1), p. 215, 2001.

Hoffmann, K., Fernandoy, F., Meyer, H., Thomas, E. R., Aliaga, A., Tetzner, D., Freitag, J., Opel, T., Arigony-Neto, J., Göbel, C. F., Jaña, R., Rodríguez Oroz, D., Tuckwell, R., Ludlow, E., McConnell, J. R., and Schneider, C.: Stable water isotopes and accumulation rates in the Union Glacier region, West Antarctica over the last 35 years, The Cryosphere, 14, 881–904, 2020.

~~Hofton, A., Lutheke, S. B., and Blair, J. B.: Estimation of ICESat intercampaign elevation biases from comparison of lidar data in East Antarctica, Geophys. Res. Lett., 40(21), 5698–5703, 2013.~~

Howat, I. M., Porter, C., Smith, B. E., Noh, M.-J., and Morin, P.: The Reference Elevation Model of Antarctica, The Cryosphere, 13, 665-674, 2019.

Krieger, G., Moreira, A., Fiedler, H., Hajnsek, I., Werner, M., Younis, M., and Zink, M.: TanDEM-X: A satellite formation for high resolution SAR interferometry, IEEE Trans. Geosc. Rem. Sens., 45, 3317–3341, 2007.

Krieger, G., Zink, M., Bachmann, M., Bräutigam, B., Schulze, D., Martone, M., Rizzoli, P., Steinbrecher, U., Anthony, J. W., De Zan, F., Hajnsek, I., Papathanassiou, K., Kugler, F., Rodriguez Cassola, M., Younis, M., Baumgartner, S., Lopez Dekker, P., Prats, P., and Moreira, A.: TanDEM-X: a radar interferometer with two formation flying satellites, Acta Astronaut., 89, 83–98, doi:10.1016/j.actaastro.2013.03.008, 2013.

Lei, Y., Siqueira, P., and Treuhaft, R.: A dense medium electromagnetic scattering model for the InSAR correlation of snow, Radio Sci., 51, 461–480, doi:10.1002/2015RS005926, 2016.

Linow, S., Hörhold, M.W., and Freitag, J.: Grain-size evolution of polar firn: a new empirical grain growth parameterization based on X-ray microcomputer tomography measurements, J. Glaciol., 58(212), 1245 – 1252, 2012.

Leinss, S., Löwe, H., Proksch, M., Lemmetyinen, J., Wiesmann, A., and Hajnsek, I.: Anisotropy of seasonal snow measured by polarimetric phase differences in radar time series, The Cryosphere,10, 1771–1797, https://doi.org/10.5194/tc-10-1771-2016, 2016.

Löwe, H., and Picard, G.: Microwave scattering coefficient of snow in MEMLS and DMRT-ML revisited: the relevance of sticky hard spheres and tomography-based estimates of stickiness, The Cryosphere, 9, 2101–2117, 2015.

Mätzler, C.: Microwave permittivity of dry snow, IEEE Trans. Geosc. Rem. Sens., 34(2), 573 – 581, 1996.

~~Nghiem, S. V., Kwok, R., Kong, J. A., and Shin, R. T.: A model with ellipsoidal scatterers for polarimetric remote sensing of anisotropic layered media, Radio Science, 28 (5), 687–703, 1993.~~

Nuth, C., and Kääb, A.: Co-registration and bias corrections of satellite elevation data sets for quantifying glacier thickness change, The Cryosphere, 5, 271–290, https://doi.org/10.5194/tc-5-271-2011, 2011.

~~Parrella, G., Hajnsek, I., and Papathanassiou, K.P.: Polarimetric decomposition of L-band PolSAR backscattering over the Austfonna ice cap, IEEE Trans. Geosc. Rem. Sens., 54 (3), 1267–1281, 2016.~~

Picard, G., Sandells, M., and Löwe, H.: SMRT: an active–passive microwave radiative transfer model for snow with multiple microstructure and scattering formulations (v1.0), Geosci. Model Dev., 11, 2763–2788, 2018.

~~Rick, U., and Albert,, M. R.: Microstructure and permeability in the near-surface firn near a potential US deep-drilling site in West Antarctica, Ann. Glac., 39, 62-66, 2004.~~

Rivera, A., Zamora, R., Rada, C., Walton, J., and Proctor, S.: Glaciological investigations on Union Glacier, Ellsworth Mountains, West Antarctica, Ann. Glaciol., 51, 91–96, 2010.

Rivera, A., Zamora, R., Jaña, R., and Oberreuter, R.: Recent ice dynamic and surface mass balance of Union Glacier in the West Antarctic Ice Sheet, The Cryosphere, 8, 1445–1456, 2014.

Rizzoli, P., Martone, M., Rott, H., and Moreira, A.: Characterization of snow facies on the Greenland Ice Sheet observed by TanDEM-X interferometric SAR data, Remote Sens., 9 (4), 315; doi:10.3390/rs9040315, 2017a.

Rizzoli, P., Martone, M., Gonzalez, C., Wecklich, C., Tridon, D. B., Bräutigam, B., Bachmann, M., Schulze, D., Fritz, T., Huber, M., Wessel, B., Krieger, G., Zink, M., and Moreira, A.: Generation and performance assessment of the global TanDEM-X digital elevation model, ISPRS J. Photogramm. Remote Sens., 132, 119–139, 2017b.

Rossi, C., Rodriguez Gonzalez, F., Fritz, T., Yague-Martinez, N., and Eineder, M.: TanDEM-X calibrated Raw DEM generation, ISPRS J. Photogrammet. Remote Sens., 73, 12 - 20, doi: 10.1016/j.isprsjprs.2012.05.014, 2012.

Rott, H., Sturm, K., and Miller, H.: Active and passive microwave signatures of Antarctic firn by means of field measurements and satellite data, Ann. Glaciol., 17, 337-343, 1993.

Feldfunktion geändert

Feldfunktion geändert

~~Rott, H., Abdel Jaber, W., Wuite, J., Scheiblauer, S., Floricioiu, D., van Wessem, J. M., Nagler, T., Miranda, N., and van den Broeke, M. R.: Changing pattern of ice flow and mass balance for glaciers discharging into the Larsen A and B embayments, Antarctic Peninsula, 2011 to 2016, The Cryosphere, 12, 1273-1291, https://doi.org/10.5194/tc-12-1272-2018, 2018.~~

Smith, B., Fricker, H. A., Gardner, A., Siegfried, M. R., Adusumilli, S., Csathó, B. M., Holschuh, N., Nilsson, J., Paolo F. S., and the ICESat-2 Science Team. *ATLAS/ICESat-2 L3A Land Ice Height, Version 2*, subset: ATL06_ATLAS/ICESat-2 L3A Glacier Elevation/Ice Sheet Elevation (HDF5). Boulder, Colorado, USA. NSIDC: National Snow and Ice Data Center, https://doi.org/10.5067/ATLAS/ATL06.002 (date accessed: 25 June 2019), 2019a.

Smith, B., Fricker, H. A., Holschuh, N., Gardner, A. S., Adusumilli, S., Brunt, K. M., Csatho, B., Harbeck, K., Huth, A., Neumann, T., Nilsson, J., and Siegfried, M. R.: Land ice height-retrieval algorithms for NASA's ICESat-2 photon-counting laser altimeter, Remote Sens. Environ., 190, 260-273, 2019b.

Tan, S., Zhu, J., Tsang, L., and Nghiem, S. V.: Microwave signatures of snow cover using numerical Maxwell equations based on discrete dipole approximation in bicontinuous media and half-space Dyadic Green's function, IEEE J. Sel. Topics Applied Earth Obs. Rem. Sens., 10, (11), 4686-4702, 2017.

Tsang, L., Pan, J., Liand, D., Li, Z., Cline, D. W., and Tan, Y.: Modeling active microwave remote sensing of snow using dense medium radiative transfer (DMRT) theory with multiple-scattering effects, IEEE Trans. Geosci. Rem. Sens., 45, 990-1004, 2007.

Tsang, L., K. H. Ding, S. Huang, and Xu, X: Electromagnetic computation in scattering of electromagnetic waves by random rough surface and dense media in microwave remote sensing of land surfaces, Proc. IEEE, 101 (2), 255–279, 2013.

Uribe, J., Zamora, R., Gacitúa, G., Rivera, A., and Ulloa, D.: A low power consumption radar system for measuring ice thickness and snow/firn accumulation in Antarctica, Ann. Glaciol., 55, 39–48, 2014.

Wessel, B., Bertram, A., Gruber, A., Bemm, S., and Dech, S.: A new high-resolution elevation model of Greenland derived from TanDEM-X, in: Proc. of the ISPRS Annals of the Photogrammetry, Remote Sensing and Spatial Information Sciences of the XXIII ISPRS Congress, Prague, Czech Republic, 12–19 July 2016, 9–16, 2016.

West, R. D., Winebrenner, D. P., Tsang, L., and Rott, H.: Microwave emission from density-stratified Antarctic firn at 6 cm wavelength, J. Glaciol., 42(140), 63-76, 1996.

Zwally, H. J., Li, J., Brenner, A. C., Beckley, M., Cornejo, H. G., DiMarzio, J., Giovinetto, M. B., Neumann, T. A., Robbins, J., Saba, J. L., Yi, D., and Wang, W.: Greenland ice sheet mass balance: distribution of increased mass loss with climate warming, J. Glaciol., 57(201), 88–102, 2011.

Zwally, H. J., Schutz, R., Bentley, C., Bufton, J., Herring, T., Minster, J., Spinhirne, J., and Thomas, R.: *GLAS/ICESat L2 Global Land Surface Altimetry Data, Version 34*, subset: 0GLAH12 GLAS/ICESat L2 Global Antarctic and Greenland Ice Sheet Altimetry Data (HDF5). Boulder, Colorado USA, NASA National Snow and Ice Data Center, Distributed Archive Center. https://dx.doi.org/10.5067/ICESAT/GLAS/DATA125 (date accessed: 28 April 2017), 2014.

Feldfunktion geändert

Feldfunktion geändert